

See discussions, stats, and author profiles for this publication at: <https://www.researchgate.net/publication/24270225>

# Evidence for Novel $\beta$ -Sheet Structures in Iowa Mutant $\beta$ -Amyloid Fibrils

ARTICLE *in* BIOCHEMISTRY · MAY 2009

Impact Factor: 3.02 · DOI: 10.1021/bi9002666 · Source: PubMed

---

CITATIONS

85

READS

22

## 4 AUTHORS, INCLUDING:



[Joseph P R O Orgel](#)

Illinois Institute of Technology

55 PUBLICATIONS 1,552 CITATIONS

[SEE PROFILE](#)



# NIH Public Access

## Author Manuscript

*Biochemistry*. Author manuscript; available in PMC 2010 July 27.

Published in final edited form as:  
*Biochemistry*. 2009 July 7; 48(26): 6072–6084. doi:10.1021/bi9002666.

## Evidence for Novel $\beta$ -Sheet Structures in Iowa Mutant $\beta$ -Amyloid Fibrils<sup>†</sup>

Robert Tycko<sup>‡</sup>, Kimberly L. Sciarretta<sup>§</sup>, Joseph P. R. O. Orgel<sup>||</sup>, and Stephen C. Meredith<sup>\*, †</sup>

<sup>‡</sup>Laboratory of Chemical Physics, National Institute of Diabetes and Digestive and Kidney Diseases, National Institutes of Health, Bethesda, Maryland 20892-0520

<sup>§</sup>Department of Molecular Genetics and Cell Biology, The University of Chicago, Chicago, Illinois 60637

<sup>||</sup>BioCAT and  $\mu$ CoSM, Pritzker Institute of Biomedical Science and Engineering, and CSRRI and Department of Biological Chemical and Physical Sciences, Illinois Institute of Technology, Chicago, Illinois 60616

<sup>\*</sup>Department of Pathology and Department of Biochemistry and Molecular Biology, The University of Chicago, Chicago, Illinois 60637

### Abstract

Asp23-to-Asn mutation within the coding sequence of  $\beta$ -amyloid, called the Iowa mutation, is associated with early onset, familial Alzheimer's disease and cerebral amyloid angiopathy, in which patients develop neuritic plaques and massive vascular deposition predominantly of the mutant peptide. We examined the mutant peptide, D23N-A $\beta$ 40, by electron microscopy, X-ray diffraction, and solid-state NMR spectroscopy. D23N-A $\beta$ 40 forms fibrils considerably faster than the wild-type peptide ( $k = 3.77 \times 10^{-3} \text{ min}^{-1}$  and  $1.07 \times 10^{-4} \text{ min}^{-1}$  for D23N-A $\beta$ 40 and the wild-type peptide WT-A $\beta$ 40, respectively) and without a lag phase. Electron microscopy shows that D23N-A $\beta$ 40 forms fibrils with multiple morphologies. X-ray fiber diffraction shows a cross- $\beta$  pattern, with a sharp reflection at  $4.7 \text{ \AA}$  and a broad reflection at  $9.4 \text{ \AA}$ , which is notably smaller than the value for WT-A $\beta$ 40 fibrils ( $10.4 \text{ \AA}$ ). Solid-state NMR measurements indicate molecular level polymorphism of the fibrils, with only a minority of D23N-A $\beta$ 40 fibrils containing the in-register, parallel  $\beta$ -sheet structure commonly found in WT-A $\beta$ 40 fibrils and most other amyloid fibrils. Antiparallel  $\beta$ -sheet structures in the majority of fibrils are indicated by measurements of intermolecular distances through  $^{13}\text{C}$ - $^{13}\text{C}$  and  $^{15}\text{N}$ - $^{13}\text{C}$  dipole-dipole couplings. An intriguing possibility exists that there is a relationship between the aberrant structure of D23N-A $\beta$ 40 fibrils and the unusual vasculotropic clinical picture in these patients.

---

The aggregation of  $\beta$ -amyloid (A $\beta$ ) peptides is believed to be essential to the pathogenesis of Alzheimer's disease (AD). Protein aggregation is also believed to underlie many other neurodegenerative diseases, as well as diseases outside the nervous system, including type II

---

<sup>†</sup>We acknowledge support from the NIH (NS042852, S.C.M.) and the Alzheimer's Association (IIRG-06-27794, S.C.M.) and from NIH Cardiovascular Pathophysiology Training Grant (HL07237, K.L.S.) and NSF (MCB-0644015 CAREER, J.P.R.O.O.). This work was supported in part by the Intramural Research Program of the National Institute of Diabetes and Digestive and Kidney Diseases of the National Institutes of Health. Use of the Advanced Photon Source was supported by the U.S. Department of Energy, Basic Energy Sciences, Office of Science, under Contract W-31-109-ENG-38. BioCAT is a National Institutes of Health-supported Research Center RR-08630.

© XXXX American Chemical Society

\*To whom correspondence should be addressed. Phone: 773-702-1267. Fax: 773-834-5251. scmeredi@uchicago.edu.

diabetes, several familial cardiomyopathies, and familial polyneuropathies. One of the strongest pieces of evidence linking A $\beta$  aggregation to the pathogenesis of AD is the occurrence of rare mutations in the  $\beta$ -amyloid precursor protein. Some of these mutations lie in sequences at or near the cleavage site for  $\beta$ - or  $\gamma$ -secretase and lead to an increase in production of A $\beta$  peptides. Several other rare mutations occur within the sequence of A $\beta$  and lead either to accelerated forms of AD or to syndromes associated with increased vascular deposition of A $\beta$ .

Solid-state NMR and electron paramagnetic resonance experiments have shown that wild-type A $\beta$  fibrils, including fibrils formed by the 40-residue A $\beta$ 40 and the 42-residue A $\beta$ 42 peptides, as well as fibrils formed by residues 10-35 of A $\beta$ , all form inregister, parallel  $\beta$ -sheets, a structure that is common to most amyloid fibrils (1-12). To date, amyloid fibrils with antiparallel  $\beta$ -sheets have been identified only for relatively short peptides that contain a single  $\beta$ -strand segment (13-16). Fibrils with out-of-register parallel  $\beta$ -sheets have not been identified. Although wild-type A $\beta$ 40 fibrils (WT-A $\beta$ 40) are polymorphic (6,17), molecular structural differences among WT-A $\beta$ 40 polymorphs do not include deviations from the in-register, parallel  $\beta$ -sheet structure (6,7).

Solid-state NMR studies of WT-A $\beta$ 40 fibrils indicate two  $\beta$ -strand segments, roughly residues 10-22 and 30-40, separated by a non- $\beta$ -sheet “bend region”. The bend region appears from solid-state NMR and other indications to be an ordered structure. For example, in WT-A $\beta$ 40 fibrils with a “striated ribbon” morphology, a salt bridge occurs between the side chains of Asp23 and Lys28 (18,19), and NMR lines of other residues in this region are strong and relatively narrow (18,20). Most A $\beta$  mutations associated with familial AD occur at or near this bend region, in residues 21-23 (21-33). We have also shown that folding of the bend region is a critical or rate-limiting step in the fibrillogenesis of at least one form of A $\beta$  fibrils (20). Thus, these mutations are of interest not only in their own right but also because they may be informative as to the folding and aggregation of wild-type A $\beta$ .

In this paper, we report investigations of the fibrillogenesis and structural organization of fibrils formed by the Iowa mutant of A $\beta$ 40, i.e., D23N-A $\beta$ 40. Electron microscopy and solid-state NMR data show that D23N-A $\beta$ 40 fibrils are polymorphic. The solid-state NMR data are strikingly inconsistent with the standard in-register, parallel  $\beta$ -sheet structure, with only approximately one-third of our D23N-A $\beta$ 40 fibrils having this structure. The majority of D23N-A $\beta$ 40 fibrils in our samples have an antiparallel  $\beta$ -sheet structure, qualitatively different from fibril structures that have been observed previously in all cases in which the fibril-forming peptide or protein is longer than 15 residues. This finding suggests a possible connection between fibril structure and disease phenotype.

## MATERIALS AND METHODS

### Peptide Synthesis and Purification

WT-A $\beta$ 40 ( $\text{NH}_2$ -DAEFRHDSGY<sup>10</sup>EVHHQKLVFF<sup>20</sup>AEDVGSNKGA<sup>30</sup>IIGL MVG GVV<sup>40</sup>-COOH) was synthesized on a 0.25 mmol scale using modified 9-fluorenylmethoxycarbonyl (FMOC) and HBTU/HOBt (Fastmoc) chemistry on an Applied Biosystems (Foster City, CA) model 433A instrument. Peptides were cleaved from the resin using 9 mL of TFA plus 0.5 mL of thioanisole, 0.3 mL of EDT, and 0.2 mL of anisole for 1.5 h at 22 °C. Peptides were purified by RP-HPLC on a preparative C18 (Zorbax) column at 60 °C. Peptide purity was greater than 98% by analytical HPLC. The molecular mass of the peptide was verified by ESI and MALDI-TOF mass spectrometry. D23N-A $\beta$ 40 was synthesized as above, except that Asn was put in place of the Asp residue at position 23.

For solid-state NMR, WT-A $\beta$ 40 and D23N-A $\beta$ 40 fibrils were prepared with  $^{13}\text{C}$  and  $^{15}\text{N}$  labels in various combinations, using isotopically labeled amino acids from Cambridge Isotopes Laboratories. Solid-state NMR samples included WT-A $\beta$ 40 with  $^{15}\text{N}$  at Phe20, WT-A $\beta$ 40 with  $^{13}\text{C}$  at the Phe19 carbonyl, D23N-A $\beta$ 40 with  $^{13}\text{C}$  at the Ala21 methyl and Val36 carbonyl and  $^{15}\text{N}$  at Leu17, D23N-A $\beta$ 40 with  $^{15}\text{N}$  at Phe20, D23N-A $\beta$ 40 with  $^{13}\text{C}$  at carbonyl sites of Leu17, Val18, Phe19, Phe20, or Ala21 carbonyl (five separate peptide samples), and D23N-A $\beta$ 40 with uniform  $^{15}\text{N}$  and  $^{13}\text{C}$  labeling of Phe19, Glu22, Val24, Gly25, Lys28, Ile31, and Leu34. For rotational echo double resonance (REDOR) experiments, peptides with  $^{15}\text{N}$  at Phe20 were mixed with peptides with  $^{13}\text{C}$  at specific carbonyl sites in a 1:1 ratio before fibrillization. All syntheses were carried out with identical conditions, except that synthesis of D23N-A $\beta$ 40 with uniformly labeled residues was performed on a 0.1 mmol scale. After purification, peptides were dissolved at  $\approx 50\text{ }^\circ\text{C}$  into 30:70 acetonitrile:water containing 0.1% TFA (v/v) and lyophilized as aliquots of 0.5 mg in siliconized 1.5 mL tubes and then stored at  $-20\text{ }^\circ\text{C}$ .

### Kinetics of Fibrillogenesis

To initiate fibrillogenesis, peptide was first dissolved in DMSO (20) and then diluted into 10 mM sodium phosphate, so that the final concentration of DMSO was  $\leq 2\%$  and the peptide concentration was approximately 100  $\mu\text{M}$ . To verify the peptide concentration used in fibrillogenesis assays, peptide concentration in buffer was assessed from absorbance at 274.6 nm, using the extinction coefficient for tyrosine of  $1420\text{ M}^{-1}\text{ cm}^{-1}$ . Peptides were incubated at  $37\text{ }^\circ\text{C}$  in 10 mM sodium phosphate, pH 7.40. Fibril formation was assessed at various times by taking 10  $\mu\text{L}$  aliquots, which were then diluted into 1 mL of 10  $\mu\text{M}$  thioflavin T solution in 10 mM sodium phosphate, pH 7.40. The sample was pipetted to disperse fibrils, and fluorescence was measured at  $\lambda_{\text{EX}} = 446\text{ nm}$  and  $\lambda_{\text{EM}} = 490\text{ nm}$ , using a Hitachi F2000 fluorescence spectrophotometer. Fluorescence measurements were made after a 3 s delay and were averaged for 10 s, using a bandwidth of 10 nm and a photomultiplier voltage of 700.

### Electron Microscopy

Images were recorded with an FEI Morgagni transmission electron microscope (TEM) operating at 80 kV. An aliquot of fibrillized peptide solution was diluted 5 $\times$  in deionized water. A 10  $\mu\text{L}$  drop was adsorbed for 120 s to a glow-discharged carbon film, supported by lacey carbon on a 300 mesh copper TEM grid. The grid was blotted, rinsed twice with deionized water, stained with 10  $\mu\text{L}$  of 3% uranyl acetate for 30 s, then blotted, dried in air, and examined in the TEM.

For measurements of fibril diameter, 5  $\mu\text{L}$  aliquots of fibril slurries of A $\beta$  D23N or wild-type A $\beta$  peptides were applied to a glow-discharged, 1-400 mesh, carbon-coated support film, washed with water, and stained with 1% uranyl acetate for 30 s. Micrographs were recorded using a FEI Tecnai F30 electron microscope at magnifications of 15000 $\times$  and 98000 $\times$ . In addition, the CCD camera added a magnification of 1.4 $\times$  to all images. Fibril diameters were measured using the “measure” tool in Adobe Photoshop 7.0 software and calibrated using scale bars incorporated into the photomicrographs. Four hundred separate measurements were made on micrographs of each type of fibril. For making histograms of the diameters, the appropriate number of bins,  $k$ , was estimated by the relationship  $k = \min\{\sqrt{n}, 10 \ln(n)/\ln(10)\}$ , where  $n$  is the sample size, i.e., 400. From this calculation, the appropriate bin size was found to be  $\sim 0.6\text{--}0.8\text{ nm}$ . A similar number was also obtained using the Scott criterion:

$$W=3.49\sigma N^{-1/3}$$

where  $W$  = optimal bin size,  $\sigma$  is the standard deviation, and  $N$  is the number of determinations (34). As will be described below, the histogram of fibril diameters appeared to have modes corresponding to two, somewhat skewed Gaussian distributions. From the means and standard deviations of the two Gaussians, a theoretical curve for the Gaussians was calculated using the relationship:

$$\frac{1}{\sigma \sqrt{2\pi}} \exp\left(-\frac{(x - \mu)^2}{2\sigma^2}\right)$$

where  $\mu$  is the mean and  $\sigma$  is the standard deviation of the distribution.

### X-ray Fiber Diffraction

Fibrils of D23N-A $\beta$ 40 and WT-A $\beta$ 40 were made in 10 mM phosphate buffer, pH 7.40, as described above. Salt was removed from the fibril samples by dialysis against water, using Spectra/Por CE MWCO 500. After centrifugation of the fibrils for 30 min at 13200g, the supernatant was removed, and the fibril slurry in the precipitate was put into 0.7 mm glass capillaries (Charles Supper). To distinguish between equatorial and meridional reflections, the capillary was placed inside a 11.7 T NMR magnet for 5 days to achieve partial alignment of the fibrils (35,36). After magnetic alignment, the fibrils formed a band with their longitudinal axis parallel to the long axis of the capillary tube. The orientation of the fibrils was determined by inspection of the fibrils by light and electron microscopy.

Synchrotron data were collected at Argonne National Laboratory, Advanced Photon Source beamline BioCAT (insertion device station) on a CCD-based X-ray detector (PCCD 168080, / Aviex/ L.L.C), where the X-ray wavelength was 1.03 Å. The sample-to-detector distance was 100 mm. X-ray diffraction data were analyzed with FIT2D ([http://www.esrf.fr/computing/expg/subgroups/data\\_analysis/FIT2D](http://www.esrf.fr/computing/expg/subgroups/data_analysis/FIT2D)). Background images were collected for the same exposure times (2 s) as the sample data collection and subtracted using the “subtraction” function of FIT2D, and the rotation (Azimuth) scans were performed with the “cake” d-scan function of FIT2D.

### Solid-State NMR

Fibrils were grown as described above for at least 8 days. Both thioflavin T measurements and TEM images were taken to monitor fibril growth. Fibrils were then dialyzed against Milli-Q water, using dialysis tubing with a molecular weight cutoff of 500, and centrifuged at 13200 rpm for 30 min in siliconized Eppendorf tubes. Pellets were resuspended in a total of 400  $\mu$ L of the supernatant and then centrifuged again (13200 rpm, 30 min). The final pellet was flash frozen, and the sample was lyophilized. Lyophilized samples (approximately 5 mg each) were packed into 3.2 mm magic angle spinning (MAS) rotors with Teflon spacers to contain the samples in the center of the NMR solenoid coil. For certain experiments, samples were rehydrated within the MAS rotors by addition of 10 mM phosphate buffer (approximately 1  $\mu$ L/mg of fibrils). One sample of  $^{15}\text{N}$ -Phe20-labeled D23N-A $\beta$ 40 fibrils was prepared by centrifugation of the wet fibril pellet directly into the MAS rotor, without lyophilization.

Solid-state NMR measurements were performed at 9.4 T (100.4 MHz  $^{13}\text{C}$  NMR frequency, 40.5 MHz  $^{15}\text{N}$  NMR frequency) and 14.1 T (150.7 MHz  $^{13}\text{C}$  NMR frequency, 60.7 MHz  $^{15}\text{N}$  NMR frequency), using three-channel 3.2 mm MAS probes (Varian) and Varian InfinityPlus spectrometer consoles. One-dimensional (1D) spectra were obtained with standard cross-polarization and two-pulse phase modulated (TPPM) proton decoupling (37) with proton radio-frequency (rf) field strengths of 100-120 kHz. Measurements of  $^{13}\text{C}$ - $^{13}\text{C}$

dipole-dipole couplings were performed at 9.4 T and 20.00 kHz MAS frequency, using the PITHIRDS-CT recoupling technique (38) or the fpRFDR-CT recoupling technique (3,39) as previously described. Measurements of  $^{15}\text{N}$ - $^{13}\text{C}$  dipole-dipole couplings were performed at 14.1 T and 7.50 kHz MAS frequency, using a version of  $^{13}\text{C}$ -detected REDOR (40,41) in which one  $\pi$  pulse per MAS rotation period was applied to both the  $^{13}\text{C}$  (at the beginning of each period) and the  $^{15}\text{N}$  (in the middle of each period) channels.  $^{13}\text{C}$  NMR signals without  $^{15}\text{N}$ - $^{13}\text{C}$  dephasing ( $S_0$  signals) and with  $^{15}\text{N}$ - $^{13}\text{C}$  dephasing ( $S_1$  signals) differed only by the application of a single  $^{15}\text{N}$   $\pi$  pulse at the midpoint of the REDOR pulse sequence. Rf pulses were actively synchronized with an MAS tachometer signal in PITHIRDS-CT, fpRFDR-CT, and REDOR measurements.  $^{13}\text{C}$  and  $^{15}\text{N}$   $\pi$  pulse lengths were 10.0 and 12.0  $\mu\text{s}$ , respectively. Frequency-selective REDOR (fsREDOR) measurements were performed at 14.1 T, using the technique of Jaroniec et al. (42) as previously described (19).

The sensitivity of REDOR (except as noted below) and fpRFDR-CT measurements was enhanced by pulsed spin-locking (PSL) (43), a technique that increases the signal-to-noise ratio by removing inhomogeneous broadening and resonance offsets during detection of  $^{13}\text{C}$  NMR signals. Typically, PSL reduces experimental measurement times by factors of 10-30, enabling measurements that would otherwise be precluded by low signal-to-noise ratio. However, signal components with small  $^{13}\text{C}$  chemical shift differences cannot be resolved under PSL detection.

Two-dimensional (2D)  $^{13}\text{C}$ - $^{13}\text{C}$  NMR spectra were recorded at 14.1 T, either at 21.5 kHz MAS frequency with finite-pulse radio-frequency-driven recoupling (fpRFDR) (44,45) and 15.0  $\mu\text{s}$   $^{13}\text{C}$   $\pi$  pulses for 2.322 ms during the mixing period or at 19.0 kHz MAS with rf-assisted diffusion (RAD) (46,47) for 500 ms during the mixing period.

$^{13}\text{C}$  chemical shifts are relative to tetramethylsilane, using the carbonyl signal of L-alanine powder at 177.95 ppm as an external reference.  $^{15}\text{N}$  chemical shifts are relative to liquid  $\text{NH}_3$ , using a ratio of 0.4029075 between the  $\text{NH}_3$  and L-alanine NMR frequencies.

## RESULTS

### Thioflavin T Fluorescence Indicates Rapid Fibril Formation by D23N-A $\beta$ 40

The kinetics of fibrillogenesis of D23N-A $\beta$ 40, monitored by thioflavin T fluorescence, are shown in Figure 1A. Fibril formation by D23N-A $\beta$ 40 shows no obvious lag period, even when fluorescence was monitored within the first hour of peptide incubation. Data in Figure 1A are well fit by the expression  $F(t) = F(0) + [F(\infty) - F(0)][1 - \exp(-kt)^n]$ , with  $n = 1$  and  $k = 3.77 \times 10^{-3} \text{ min}^{-1}$ . As described previously (20), kinetics of WT-A $\beta$ 40 fibrillogenesis can be fit to the same form, but with  $n = 2.24 \pm 0.37$  and  $k = 1.07 \times 10^{-4} \text{ min}^{-1}$ . With  $n > 1$ , this expression is a stretched exponential, with a lag period that precedes the onset of fluorescence enhancement. These results are in reasonable agreement with earlier observations of van Nostrand et al. (22), who observed more rapid fibril formation by D23N-A $\beta$ 40 than by WT-A $\beta$ 40.

Lactam cross-linking of D23 and K28 side chains in WT-A $\beta$ 40 has been shown previously to eliminate the lag period in thioflavin T fluorescence measurements (20), suggesting that constraining the conformation of residues 23-28 greatly accelerates fibril nucleation or fibril growth. Apparently, the D23N substitution has a similar effect, perhaps also by restricting the conformational freedom in residues 23-28.

## Electron Microscopy Indicates Multiple D23N-A $\beta$ 40 Fibril Structures

Panels B-D of Figure 1 show negatively stained TEM images of D23N-A $\beta$ 40 fibrils. These fibrils have diameters, lengths, and the straight, unbranched appearance that are typical of amyloid fibrils. Close examination of the images reveals coexistence of several structures, including fibrils with an apparent, approximately periodic twist (single-headed arrows) and fibrils that lack an apparent twist (double-headed arrows). Untwisted fibrils occur either as single filaments or as what appear to be laterally associated pairs of filaments. Similar twisted and untwisted structures have been described previously for WT-A $\beta$ 40 fibrils and have been shown to arise from distinct molecular structures (6,7,16). From these images of D23N-A $\beta$ 40 fibrils, there appear to be at least two distinct molecular structures for D23N-A $\beta$ 40 fibrils, corresponding to the twisted and untwisted morphologies. Coexistence of more than two D23N-A $\beta$ 40 fibril structures in our samples is not inconsistent with the TEM images, as neither the twisted nor the untwisted fibrils are clearly structurally homogeneous.

The diameters of D23N-A $\beta$ 40 fibrils also showed heterogeneity, with two distinct modes in the histograms of fibril diameters (Supporting Information Figure 1). The minority population of D23N-A $\beta$ 40 fibrils had a mean diameter of  $11.20 \pm 1.42$  nm (mean  $\pm$  SD), approximately the same as wild-type A $\beta$ 40 fibrils ( $11.15 \pm 0.85$  nm, mean  $\pm$  SD). The majority of D23N-A $\beta$ 40 fibrils, however, were consistently smaller, with diameters of  $6.90 \pm 2.26$  nm (mean  $\pm$  SD).

## X-ray Fiber Diffraction Indicates Structural Differences between D23N-A $\beta$ 40 and WT-A $\beta$ 40 Fibrils

Figure 2 compares X-ray fiber diffraction patterns of partially aligned D23N-A $\beta$ 40 (Figure 2A) and WT-A $\beta$ 40 (Figure 2B) fibrils. A “cross- $\beta$ ” diffraction pattern is observed in both cases, i.e., a sharp, meridional reflection at  $4.7$  Å, at right angles to a broad equatorial reflection of roughly  $10$  Å. The equatorial reflection for D23N-A $\beta$ 40 fibrils has its maximum at  $9.4$  Å, while that of WT-A $\beta$ 40 fibrils has its maximum at  $10.6$  Å. This difference suggests a significant difference in fibril structure, specifically in the average spacing between layers of  $\beta$ -sheets.

## One-Dimensional Solid-State NMR Spectra Indicate the Coexistence of Three D23N-A $\beta$ 40 Fibril Structures

Panels A and B of Figure 3 show 1D  $^{13}\text{C}$  NMR spectra of D23N-A $\beta$ 40 fibrils labeled with  $^{13}\text{C}$  at the carbonyl site of Val36 and the methyl site of Ala21. In the rehydrated state (i.e., with phosphate buffer added to lyophilized fibrils in the MAS rotor), both the carbonyl and the methyl lines show three partially resolved components, suggesting coexistence of three distinct structural environments for Val36 and Ala21 in the fibril sample (Figure 3A). In the dry, lyophilized state, splittings of the carbonyl and methyl lines are not resolved (Figure 3B), due to the increased line widths that are commonly observed and attributed to greater static disorder in lyophilized fibrils (14,48). In view of the polymorphism in TEM images, the simplest explanation for these NMR signals is that three D23N-A $\beta$ 40 fibril structures are present in the sample, with comparable abundances. We discount the alternative explanation that the three Val36 and Ala21 environments might be present within a single fibril structure on the grounds that a single fibril structure would not produce the observed variety of fibril morphologies in TEM images, especially as studies of WT-A $\beta$ 40 fibrils have established clear connections between morphology in TEM images and underlying molecular structure. Other solid-state NMR data described below are also inconsistent with a single fibril structure. Although the possibility exists that one fibril structure might contain two distinct structural environments for Val36 and Ala21 (with another fibril structure containing one structural environment), all detailed structural models for amyloid fibrils that have been developed to date (7,12,19,49) have a single molecule in

the asymmetric unit (i.e., a single structural environment). A fibril structure with two molecules in the asymmetric unit (i.e., two structural environments for D23N-A $\beta$ 40 molecules within a single fibril) therefore seems unlikely.

Figure 3C shows the  $^{13}\text{C}$  NMR spectrum of D23N-A $\beta$ 40 fibrils prepared from a 1:1 mixture of peptides labeled with  $^{13}\text{C}$  at the carbonyl site of Phe19 and peptides labeled with  $^{15}\text{N}$  at Phe20. (Mixtures of  $^{15}\text{N}$ - and  $^{13}\text{C}$ -labeled peptides were used also for REDOR experiments to examine  $\beta$ -sheet register, as discussed below.) Again, the carbonyl NMR signal shows three partially resolved components in the rehydrated D23N-A $\beta$ 40 fibrils. In contrast, the  $^{13}\text{C}$  NMR spectrum of rehydrated WT-A $\beta$ 40 fibrils prepared from a 1:1 mixture of peptides with the same isotopic labels (Figure 3D) does not show a splitting of the carbonyl NMR signal.

Figure 3E shows carbonyl regions of  $^{13}\text{C}$  NMR spectra of D23N-A $\beta$ 40 fibrils prepared from 1:1 mixtures of peptides labeled with  $^{13}\text{C}$  at the carbonyl site of Leu17, Val18, Phe19, Phe20, or Ala21 and peptides labeled with  $^{15}\text{N}$  at Phe20, recorded in the lyophilized state without rehydration. Line widths for carbonyl signals (full width at half-maximum, fwhm) range from 2.5 ppm (Ala21) to 5.0 ppm (Phe20). For comparison, carbonyl line widths for lyophilized WT-A $\beta$ 40 fibrils with a single morphology are typically narrower, i.e., less than 2.5 ppm (6).

$^{13}\text{C}$  chemical shifts for all carbonyl sites in Figure 3 are more than 1.0 ppm upfield from the corresponding random coil shifts (50), as expected for carbonyl sites in  $\beta$ -strand segments (see Table 1).  $^{13}\text{C}$  chemical shifts for the Ala21 methyl site are more than 2.5 ppm downfield from the corresponding random coil shift, again as expected for alanines in  $\beta$ -strand segments. Thus, the  $^{13}\text{C}$  chemical shifts for all D23N-A $\beta$ 40 fibril structures in our samples are consistent with the strand-bend-strand conformational motif identified previously in WT-A $\beta$ 40 fibrils (7,18,19).

Figure 4A shows 1D  $^{15}\text{N}$  spectra of a D23N-A $\beta$ 40 fibril sample that was  $^{15}\text{N}$ -labeled at Phe20 and examined in a fully hydrated state, without lyophilization. Two resolved lines with an approximate 1:2 ratio of areas are observed, at 129.5 and 123.0 ppm. We attribute the weaker  $^{15}\text{N}$  line to one of the three fibril structures indicated by the  $^{13}\text{C}$  NMR data in Figure 3 and the stronger line to the other two structures, although we cannot make specific correlations between the  $^{15}\text{N}$  and the  $^{13}\text{C}$  signals from available data. A similar spectrum is observed for rehydrated fibrils labeled with  $^{15}\text{N}$  at Phe20 and  $^{13}\text{C}$  at the Phe19 carbonyl site (1:1 peptide mixture, Figure 4B). Similar spectra are also observed for lyophilized fibrils (Figure 4D), although the  $^{15}\text{N}$  NMR lines are somewhat broader in the lyophilized state. Area ratios for the two components range from 1.3:1 to 2.0:1, attributable to variations in the relative proportions of different D23N-A $\beta$ 40 fibril structures. The fact that significant variations in these area ratios are observed supports the interpretation that different signal components are associated with different fibril structures. In contrast, the  $^{15}\text{N}$  spectrum of WT-A $\beta$ 40 fibrils labeled with  $^{15}\text{N}$  at Phe20 (Figure 4C) shows a single sharp line at 127.0 ppm.

### Anomalous Intermolecular $^{13}\text{C}$ - $^{13}\text{C}$ Distances in D23N-A $\beta$ 40 Fibrils Indicate Novel $\beta$ -Sheet Structures

Panels A and B of Figure 5 show  $^{13}\text{C}$  NMR spectra of rehydrated D23N-A $\beta$ 40 fibrils with  $^{13}\text{C}$  labels at the Ala21 methyl and Val36 carbonyl sites, recorded as a function of the effective  $^{13}\text{C}$ - $^{13}\text{C}$  dipolar evolution time  $\tau_D$  in PITHIRDS-CT measurements of intermolecular  $^{13}\text{C}$ - $^{13}\text{C}$  dipole-dipole couplings. The PITHIRDS-CT and fpRFDR-CT techniques are quite similar, and the resulting data are nearly identical, although the more recently developed PITHIRDS-CT technique involves a somewhat simpler rf pulse sequence

(38). In addition, the PITHIRDS-CT measurements were performed without PSL, so that the signal components arising from different D23N-A $\beta$ 40 fibril structures remain resolved. In both the Ala21 and Val36 data, only one of the signal components decays on the 30 ms time scale expected for intermolecular dipole-dipole couplings in an inregister, parallel  $\beta$ -sheet (3,6-9,12). Comparison with numerical simulations in Figure 5C indicates intermolecular distances of approximately 0.5 nm for the rapidly decaying signal components (labeled c and d in Figure 5) and distances greater than 0.7 nm for the other components. These data show that only approximately one-third of the D23N-A $\beta$ 40 fibrils in this sample, probably representing one of three coexisting fibril structures, have the inregister, parallel  $\beta$ -sheets identified in all previous studies of full-length  $\beta$ -amyloid peptide fibrils (3,5-7,10,19). The remaining D23N-A $\beta$ 40 fibrils have an anomalous  $\beta$ -sheet structure.

Figure 5D shows  $^{13}\text{C}$ - $^{13}\text{C}$  dipole-dipole coupling measurements for lyophilized D23N-A $\beta$ 40 fibrils labeled with  $^{15}\text{N}$  at Phe20 and  $^{13}\text{C}$  at the indicated carbonyl sites (1:1 mixtures), obtained with the fpRFDR-CT technique (3, 39). Data in Figure 5D were obtained with PSL, so that signal components from different fibril structures were not resolved. These data show that the majority of fibrils have intermolecular distances for Val18, Phe19, Phe20, and Ala21 carbonyl sites that are roughly 0.7 nm or greater. From these data alone, it is not possible to determine whether one D23N-A $\beta$ 40 fibril structure has in-register, parallel  $\beta$ -sheets.

### Intermolecular $^{15}\text{N}$ - $^{13}\text{C}$ Distances in D23N-A $\beta$ 40 Fibrils Indicate Antiparallel $\beta$ -Sheets with $17 + k \leftrightarrow 21 - k$ Registry

Figure 6A shows measurements of intermolecular  $^{15}\text{N}$ - $^{13}\text{C}$  dipole-dipole couplings (i.e.,  $^{15}\text{N}$ - $^{13}\text{C}$  distances) between Phe20 amide sites and carbonyl sites of Leu17, Val18, Phe19, Phe20, and Ala21 in D23N-A $\beta$ 40 fibrils prepared from 1:1 mixtures of  $^{15}\text{N}$ -labeled peptides and  $^{13}\text{C}$ -labeled peptides, recorded with the REDOR technique (40, 41). These are  $^{13}\text{C}$ -detected REDOR measurements. Fibril samples were lyophilized, and PSL detection was required to enhance sensitivity, so that REDOR curves for different signal components were not resolved. Clear variations in the REDOR data for different positions of the  $^{13}\text{C}$  labels are observed, with the most rapid rise of the normalized REDOR difference signal  $\Delta S/S_0$ , corresponding to the shortest  $^{15}\text{N}$ - $^{13}\text{C}$  distances, occurring when the  $^{13}\text{C}$  labels are at the Val18 carbonyl position. The longest  $^{15}\text{N}$ - $^{13}\text{C}$  distances occur when the  $^{13}\text{C}$  labels are at the Phe20 or Ala21 carbonyl position.

Solid lines in Figure 6B are simulated REDOR data for the five samples, assuming an inregister, parallel  $\beta$ -sheet structure with the idealized geometry shown in Figure 6C. The fact that the fibrils are prepared from 1:1 isotopic mixtures is taken into account by averaging simulations in which a given  $^{13}\text{C}$  label (at one of the carbonyl positions on the middle chain in Figure 6C) is coupled to two  $^{15}\text{N}$  labels (on both the upper and lower chains in Figure 6C), to one  $^{15}\text{N}$  label (on either the upper or the lower chain), or to no  $^{15}\text{N}$  labels. In addition, contributions of natural-abundance carbonyl  $^{13}\text{C}$  nuclei to the REDOR data are taken into account by multiplying the averaged REDOR curves by 0.5 (since the number of deliberate carbonyl  $^{13}\text{C}$  labels in these samples is nearly equal to the expected number of natural-abundance carbonyl  $^{13}\text{C}$  nuclei).

In these experiments, all mixtures contain  $^{15}\text{N}$ -Phe20 and one of five 1- $^{13}\text{C}$ -labeled amino acids: Leu17, Val18, Phe19, Phe20, or Ala21. Thus, for an in-register, parallel  $\beta$ -sheet, the shortest  $^{15}\text{N}$ - $^{13}\text{C}$  distance from the  $^{15}\text{N}$  label at Phe20 to a  $^{13}\text{C}$  label occurs when the  $^{13}\text{C}$  is at Phe19 (nearest-neighbor distances of 4.2 Å and 5.6 Å). That is, the backbone carbonyl group of residue  $n$  makes a hydrogen bond to the backbone amide group of residue  $n + 1$  on a neighboring peptide chain. Experimental REDOR data for WT-A $\beta$ 40 fibrils with labels at these positions are in excellent agreement with the idealized simulations for an in-register,

parallel  $\beta$ -sheet (Figure 6B). On the other hand, experimental REDOR data for D23N-A $\beta$ 40 fibrils do not agree with these simulations, again indicating anomalous  $\beta$ -sheet structures. The rapid rise of REDOR signals in Figure 6A for the D23N-A $\beta$ 40 sample with  $^{13}\text{C}$  at Val18 suggests the presence of  $\beta$ -sheets in which the Val18 carbonyl group of a given chain is hydrogen-bonded to the Phe20 amide group of a neighboring chain. Such hydrogen bonds might occur either in parallel  $\beta$ -sheets with a one-residue shift in hydrogen bond registry or in antiparallel  $\beta$ -sheets in which carbonyl groups of residue  $17 + k$  are hydrogen-bonded to amide groups of residue  $21 - k$ , with  $k$  being an integer. However, the shifted parallel  $\beta$ -sheet structure would also necessarily contain hydrogen bonds between the Phe20 carbonyl group of a given chain and the Phe20 amide group of a neighboring chain, so that there should be a strong REDOR signal for the D23N-A $\beta$ 40 sample in which both Phe20 carbonyls and Phe20 amides are labeled, contrary to the experimental data in Figure 6A.

Dashed lines in Figure 6B are simulated REDOR data for an antiparallel  $\beta$ -sheet structure with the idealized geometry shown in Figure 6D and with  $17 + k \leftrightarrow 21 - k$  hydrogen bonds. These simulations are in reasonable agreement with the experimental REDOR data for all five samples in Figure 6A. In particular, the strongest REDOR signal is for the Val18-labeled sample, followed by the Leu17- and Phe19-labeled samples. Phe20- and Ala21-labeled samples are predicted to have weak REDOR signals, as observed. Because all samples also contain a minor population of in-register, parallel  $\beta$ -sheet fibrils, exact agreement with antiparallel REDOR simulations is not expected. In structurally heterogeneous samples, experimental REDOR data may also be affected by differences in transverse nuclear spin relaxation rates among different fibril structures.

Further support for antiparallel  $\beta$ -sheets in D23N-A $\beta$ 40 fibrils comes from REDOR measurements on rehydrated fibrils with  $^{13}\text{C}$  labels at the Val36 carbonyl and Ala21 methyl sites and a  $^{15}\text{N}$  label at the Leu17 amide site (same sample as in Figures 3A,B and 5A-C), performed without PSL. As shown in Figure 7A, the two Ala21 methyl lines that do not decay rapidly in  $^{13}\text{C}$ - $^{13}\text{C}$  PITHIRDS-CT measurements (Figure 5), and hence do not arise from fibrils with in-register, parallel  $\beta$ -sheet structures, show significant  $^{15}\text{N}$ - $^{13}\text{C}$  REDOR difference signals, indicating intermolecular proximity to Leu17. The other Ala21 methyl line does not show a significant REDOR difference signal. As a control, data in Figure 7B show the absence of REDOR difference signals for all Val36 carbonyl lines, as expected since Val36 should not be near Leu17 in either parallel or antiparallel  $\beta$ -sheets. Comparisons with REDOR simulations for ideal  $17 + k \leftrightarrow 20k$ ,  $17 + k \leftrightarrow 21 - k$ , and  $17 + k \leftrightarrow 22 - k$  antiparallel  $\beta$ -sheet structures (Figure 7C) indicate that the Ala21 methyl REDOR data are consistent with either  $17 + k \leftrightarrow 20k$  or  $17 + k \leftrightarrow 21 - k$  registries of intermolecular hydrogen bonds. Together with the results in Figure 6 discussed above, our REDOR data for D23N-A $\beta$ 40 fibrils indicate that fibrils with antiparallel  $\beta$ -sheet structures have the  $17 + k \leftrightarrow 21 - k$  registry.

REDOR simulations in Figure 7C assume that each Ala21 methyl  $^{13}\text{C}$  is dipole-coupled to Leu17 amide  $^{15}\text{N}$  on both nearest-neighbor chains.  $^{15}\text{N}$ - $^{13}\text{C}$  distances extracted from antiparallel  $\beta$ -sheet models are 5.1 and 6.3 Å for  $17 + k \leftrightarrow 20k$  registry, 5.3 and 5.6 Å for  $17 + k \leftrightarrow 21k$  registry, and 6.4 and 7.4 Å for  $17 + k \leftrightarrow 22k$  registry. The similar distances for  $17 + k \leftrightarrow 20k$  and  $17 + k \leftrightarrow 21k$  registries result in similar REDOR curves. Deviations of experimental REDOR data for peak b from simulated curves may be due to partial overlap with Ala21 methyl signals from parallel  $\beta$ -sheet structures, which would reduce the experimentally determined values of  $\Delta S/S_0$ .

## Two-Dimensional Solid-State NMR Spectra Indicate Intersheet Phe19/Leu34 Contacts in D23N-A $\beta$ 40 Fibrils

Figure 8A shows the aliphatic region of a 2D  $^{13}\text{C}$ - $^{13}\text{C}$  NMR spectrum of rehydrated D23N-A $\beta$ 40 fibrils prepared with uniform  $^{15}\text{N}$  and  $^{13}\text{C}$  labeling of Phe19, Glu22, Val24, Gly25, Lys28, Ile31, and Leu34. This spectrum was obtained with a 2.232 ms mixing period of dipolar recoupling, using the fpRFDR technique (44, 45), which produces strong cross-peaks between NMR lines of directly bonded  $^{13}\text{C}$  sites. Chemical shift assignments based on one-bond cross-peaks are shown in Figure 8A. Broad cross-peaks ( $>4$  ppm fwhm) are observed for Glu22, Val24, Gly25, and Ile31, suggesting conformational variations in the bend region that may be associated with the fibril polymorphism. Narrower cross-peaks are observed for Phe19 and Leu34.

Panels B and C of Figure 8 show a 2D  $^{13}\text{C}$ - $^{13}\text{C}$  NMR spectrum of the same sample, obtained with a 500 ms RAD mixing period (46,47). Under these measurement conditions, strong cross-peaks develop among all NMR lines within a single labeled residue, and weaker cross-peaks develop among NMR lines of sequential labeled residues (e.g., Val24/Gly25 cross-peaks in Figure 8B) or nonsequential labeled residues that are in spatial proximity and hence have significant  $^{13}\text{C}$ - $^{13}\text{C}$  nuclear magnetic dipole-dipole couplings (approximately 6 Å or less distance among side chain carbon atoms). In particular, cross-peaks between Phe19 aromatic signals at 129 ppm and Leu34 aliphatic signals around 25 ppm are observed, indicating contacts between side chains of Phe19 and Leu34. Such contacts between side chains of odd-numbered residues in the first  $\beta$ -strand segment and side chains of even-numbered residues in the second  $\beta$ -strand segment have been observed previously in WT-A $\beta$ 40 fibrils (7,19). It is unclear whether these side chain-side chain contacts are present in all or only some D23N-A $\beta$ 40 fibril structures.

## Asp23-Lys28 Salt Bridges in WT-A $\beta$ 40 Fibrils Are Not Replaced by Glu22-Lys28 Salt Bridges in D23N-A $\beta$ 40 Fibrils

Previous solid-state NMR studies have shown that oppositely charged Asp23 and Lys28 side chains interact through a salt bridge in certain WT-A $\beta$ 40 fibrils, especially fibrils with a striated ribbon morphology that develop under agitated growth conditions (6,18,19). The formation of this salt bridge may be an important and even rate-limiting step for WT-A $\beta$ 40 fibril nucleation or growth, as shown by the fact that a peptide with a lactam bond between these residues undergoes fibril formation at  $\sim 10^3$ -fold faster rate (20). Since D23N-A $\beta$ 40 lacks the negative charge at the mutated position, but still has a negative charge at the adjacent residue, Glu22, we asked whether a Glu22-Lys28 salt bridge might be present in D23N-A $\beta$ 40 fibrils.

Figure 9 compares fsREDOR data for D23N-A $\beta$ 40 fibrils with fsREDOR data for striated ribbon WT-A $\beta$ 40 fibrils. These fsREDOR measurements were performed on rehydrated fibril samples with uniform  $^{15}\text{N}$ ,  $^{13}\text{C}$  labeling of multiple residues, including Lys28 and either Glu22 (for D23N-A $\beta$ 40) or Asp23 (for WT-A $\beta$ 40). For D23N-A $\beta$ 40 fibrils, no Glu22 side chain carboxyl signal is detected in the fsREDOR difference spectrum, even at the longest  $^{15}\text{N}$ - $^{13}\text{C}$  dephasing periods. For WT-A $\beta$ 40 fibrils, a strong Asp23 side chain carboxyl signal is detected in the fsREDOR difference spectrum, in agreement with earlier measurements (19). Thus, we find no evidence that side chain carboxyl groups of Glu22 are in close proximity (5 Å or less) to side chain amine groups of Lys28 in D23N-A $\beta$ 40 fibrils, i.e., no evidence for Glu22-Lys28 salt bridge interactions.

## DISCUSSION

In this paper, we described structural features of amyloid fibrils formed by an A $\beta$  peptide bearing an Asp23 → Asn point mutation (22). The proband with this mutation was a member of a three-generation Iowa family with autosomal dominant dementia beginning in the sixth or seventh decade of life (23). The symptoms in the proband and an affected brother included progressive aphasic dementia, leukoencephalopathy, and occipital calcifications. At post-mortem examination, the brain showed severe cerebral amyloid angiopathy (CAA), widespread neurofibrillary tangles, and unusually extensive distribution of A $\beta$ 40 in plaques. The plaques also were less compact and had a higher A $\beta$ 40/A $\beta$ 42 ratio than the plaque occurring in wild-type Alzheimer's disease.

The unusual phenotype of this form of familial dementia, and the presence of a structural mutation within a region of the A $\beta$  peptide that is critical in determining fibril structure, suggested to us that the fibrils and other aggregates might also have unusual features. We observed that D23N-A $\beta$ 40 formed fibrils more rapidly than WT-A $\beta$ 40, though not so rapidly as lactam(D23/K28)-A $\beta$ 40:  $k = 3.77 \times 10^{-4} \text{ min}^{-1}$ , compared to  $k = 1.07 \times 10^{-4} \text{ min}^{-1}$  for WT-A $\beta$ 40 and  $k = 0.107 \text{ min}^{-1}$  for lactam(D23/K28)-A $\beta$ 40. Moreover, D23N-A $\beta$ 40 showed no lag period in the fibrillation kinetics, and thioflavin T fluorescence values were consistently somewhat higher than those of WT-A $\beta$ 40, suggesting that D23N-A $\beta$ 40 fibrils differed structurally from WT-A $\beta$ 40 fibrils. The rapid fibrillation and lack of a lag period also suggest that structural differences in the fibrils may reflect structural differences in prefibrillar aggregates.

The possibility of structural differences from the wild-type peptide was confirmed in further studies by electron microscopy, X-ray fiber diffraction, and solid-state NMR. Electron microscopy showed abundant fibrils with multiple morphologies, the majority of which had a smaller mean diameter than typical wild-type A $\beta$ 40 fibrils. Fiber diffraction of aligned D23N-A $\beta$ 40 fibrils showed two reflections consistent with the expected cross- $\beta$  structure, but at 4.7 and 9.4 Å. The latter number is significantly smaller than the corresponding number for WT-A $\beta$ 40 fibrils grown under similar conditions (10.4 Å), suggesting that the  $\beta$ -sheets in D23N-A $\beta$ 40 fibrils are more closely packed, on average, than in WT-A $\beta$ 40 fibrils.

Solid-state NMR data for D23N-A $\beta$ 40 fibrils are striking in several respects. First, although fibril polymorphism is expected to produce multiple sets of  $^{13}\text{C}$  and  $^{15}\text{N}$  chemical shifts, the chemical shift variations in Figure 5A,B and in Figure 4 are quite large, qualitatively suggesting large structural variations. The PITHIRDS-CT and fpRFDR-CT data in Figure 5 are unprecedented. Similar measurements on WT-A $\beta$ 40 fibrils with various morphologies have always shown pronounced  $^{13}\text{C}$  signal decays on the 30 ms time scale, indicating in-register, parallel  $\beta$ -sheets (3, 6, 7), especially for  $^{13}\text{C}$ -labeled sites in residues 12-39. The significantly slower signal decays for approximately two-thirds of the  $^{13}\text{C}$  signal from all of the labeled sites in Figure 5 are strong evidence for anomalous  $\beta$ -sheet structures in D23N-A $\beta$ 40 fibrils. We emphasize that exhaustive TEM imaging of our D23N-A $\beta$ 40 samples (as in Figure 1) shows no evidence for nonfibrillar D23N-A $\beta$ 40 aggregates. Thus, we believe that all signals in Figure 5 and in other solid-state NMR experiments described above arise from fibrils.

REDOR data in Figures 6 and 7 support the existence of anomalous  $\beta$ -sheet structures, as these data indicate shorter distances between Phe20 amide sites and carbonyl sites of Leu17 and Val18 and between Leu17 amide sites and methyl sites of Ala21 than are expected in an in-register, parallel structure. The combined REDOR data support the existence of antiparallel  $\beta$ -sheets with  $17 + k \leftrightarrow 21 - k$  hydrogen bond registry in the D23N-A $\beta$ 40 fibrils that do not contain the more conventional in-register, parallel  $\beta$ -sheets. Antiparallel  $\beta$ -sheets

have not been demonstrated previously in amyloid fibrils formed by peptides longer than 15 residues.  $17 + k \leftrightarrow 21 - k$  registry has been established previously for the antiparallel  $\beta$ -sheets in fibrils formed by residues 16-22 of A $\beta$  (13,14).

Additional experiments will be required before specific structural models for D23N-A $\beta$ 40 fibrils can be developed and proven. Foremost among these experiments would be the development of fibrillization techniques that yield less heterogeneous fibril samples. Nevertheless, several pieces of data are consistent with a strand-bend-strand model, in particular, (1) the non- $\beta$ -sheet secondary chemical shift of Val24, which is also non- $\beta$ -sheet in other amyloid fibrils where the strand-bend-strand has been demonstrated from other types of data (2,7,18,19), (2) the presence of a contact between the side chains of Leu17 and Phe34, and (3) the predominant modal fibril diameter of 7 nm, which is inconsistent with a fully extended  $\beta$ -sheet and could accommodate only ~20 residues. While these data allow only for tentative conclusions, Figure 10 shows a hypothetical model that may apply to fibrils with antiparallel  $\beta$ -sheet structures. Parallel  $\beta$ -sheets favor maximization of hydrophobic interactions in A $\beta$  fibrils (5,13); in addition, Figure 10 shows how the strand-bend-strand conformational motif of A $\beta$  may also allow favorable alignment of N-terminal (residues 17-21) and C-terminal (residues 30-40) hydrophobic segments in an antiparallel  $\beta$ -sheet structure by positioning the two hydrophobic segments in separate  $\beta$ -sheet layers. The antiparallel structure may also allow favorable electrostatic interactions between oppositely charged Lys16 and Glu22 side chains and possibly between Lys28 side chains and the C-terminal carboxylate of Val40. Why the D23N substitution facilitates formation of antiparallel  $\beta$ -sheet structures and whether wild-type A $\beta$  can also adopt an antiparallel structure under certain circumstances are unresolved questions. Since amyloid fibril structures are kinetically determined at the nucleation stage rather than thermodynamically determined (6), preference for parallel or antiparallel structures in mature fibrils may be a consequence of the structural properties of mutant and wild-type peptide oligomers.

Finally, it is tempting to speculate about the possible relationship between the structure of D23N-A $\beta$ 40 fibrils and the unusual phenotype of this form of familial AD. Although neuritic plaques are increased in patients with the Iowa mutation, the dominant disease phenotype results from cerebrovascular deposition of peptide. Cerebrovascular deposition of WT-A $\beta$ 40 is also a feature associated with sporadic, late-onset AD, though this feature is usually less prominent than in patients with CAA, such as those patients with the Iowa mutation. CAA is also found in patients with other point mutations in the same coding region of  $\beta$ -amyloid, i.e., the Dutch (E22Q), Arctic (E22G), Italian (E22K), and Flemish (A21G) mutations, some of which also are associated with more typical lesions of AD such as the neuritic plaque. In addition, CAA has been described in association with mutations in the genes for other proteins, including cystatin C and transthyretin, both of which readily form fibrils. CAA is also a frequent finding in individuals with sporadic, late-onset Alzheimer's disease. It has been estimated that 30-40% of patients with CAA have AD by clinical or pathological criteria (51), and most patients with autopsy-proven AD also have some degree of histologically demonstrable CAA, often extensive (52,53). Both clinical entities are associated with the presence of the apolipoprotein E  $\epsilon 4$  allele (54). Nevertheless, there are also individuals with "pure" forms of either AD with neuritic plaques and neurofibrillary tangles or CAA (54,55).

It is not well understood how A $\beta$  peptides are partitioned between cerebrospinal fluid and blood vessels, and the receptors and transporters of these peptides are still largely uncharacterized. An intriguing possibility stems from the observation that both WT-A $\beta$ 40 fibrils and D23N-A $\beta$ 40 fibrils are polymorphic. It is possible that D23N-A $\beta$ 40 preferentially adopts a conformation that favors transport of this peptide into the vascular wall. According

to this speculative hypothesis, WT-A $\beta$ 40 can also adopt this conformation and be transported to the vascular wall but does so less often than the mutant peptide.

## Supplementary Material

Refer to Web version on PubMed Central for supplementary material.

## Acknowledgments

We thank Yimei Chen of the University of Chicago Electron Microscopy Facility and Hélène Auer and Neeraj Chopra for synthesizing several of the peptides. This work benefited from the support of the NSF Research Collaborative Network, “Fibernet” (MCB-0234001).

## Abbreviations

1D	one dimensional
2D	two dimensional
A $\beta$	$\beta$ -amyloid
AD	Alzheimer's disease
CAA	cerebral amyloid angiopathy
DMSO	dimethyl sulfoxide
EDT	ethanedithiol
ESI	electrospray ionization
FMOC	9-fluorenylmethoxycarbonyl
fpRFDR-CT	finite pulse, radio-frequency driven, constant time
fsREDOR	frequency-selective REDOR
fwhm	full width at half-maximum
HBTU	2-(1 <i>H</i> -benzotriazol-1-yl)-1,1,3,3-tetramethyluronium hexafluorophosphate
HOBT	<i>N</i> -hydroxybenzotriazole
MALDI-TOF	matrix-assisted laser desorption ionization-time of flight
MAS	magic angle spinning
MWCO	molecular weight cutoff
NMR	nuclear magnetic resonance
PITHIRDS-CT	PITHIRDS-constant time
PSL	pulsed spin-locking
REDOR	rotational echo double resonance
rf	radio frequency
RP-HPLC	reverse-phase high-performance liquid chromatography
SD	standard deviation
TEM	transmission electron microscopy
TFA	trifluoroacetic acid

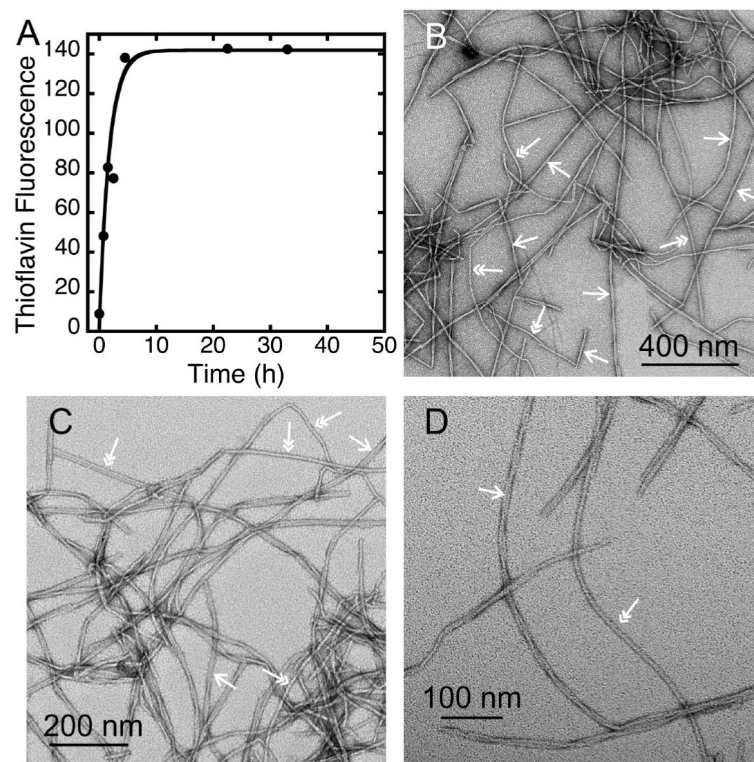
TPPM	two-pulse phase modulated
WT	wild type

## REFERENCES

1. Tycko R. Characterization of amyloid structures at the molecular level by solid state nuclear magnetic resonance spectroscopy. *Methods Enzymol* 2006;413:103–122. [PubMed: 17046393]
2. Tycko R. Molecular structure of amyloid fibrils: insights from solid state NMR. *Q. Rev. Biophys* 2006;39:1–55. [PubMed: 16772049]
3. Balbach JJ, Petkova AT, Oyler NA, Antzutkin ON, Gordon DJ, Meredith SC, Tycko R. Supramolecular structure in full-length Alzheimer's  $\beta$ -amyloid fibrils: evidence for a parallel beta-sheet organization from solid-state nuclear magnetic resonance. *Biophys. J* 2002;83:1205–1216. [PubMed: 12124300]
4. Benzinger TL, Gregory DM, Burkoth TS, Miller-Auer H, Lynn DG, Botto RE, Meredith SC. Propagating structure of Alzheimer's  $\beta$ -amyloid(10-35) is parallel  $\beta$ -sheet with residues in exact register. *Proc. Natl. Acad. Sci. U.S.A* 1998;95:13407–13412. [PubMed: 9811813]
5. Antzutkin ON, Balbach JJ, Leapman RD, Rizzo NW, Reed J, Tycko R. Multiple quantum solid-state NMR indicates a parallel, not antiparallel, organization of  $\beta$ -sheets in Alzheimer's  $\beta$ -amyloid fibrils. *Proc. Natl. Acad. Sci. U.S.A* 2000;97:13045–13050. [PubMed: 11069287]
6. Petkova AT, Leapman RD, Guo ZH, Yau WM, Mattson MP, Tycko R. Self-propagating, molecular-level polymorphism in Alzheimer's  $\beta$ -amyloid fibrils. *Science* 2005;307:262–265. [PubMed: 15653506]
7. Paravastu AK, Leapman RD, Yau WM, Tycko R. Molecular structural basis for polymorphism in Alzheimer's  $\beta$ -amyloid fibrils. *Proc. Natl. Acad. Sci. U.S.A* 2008;105:18349–18354. [PubMed: 19015532]
8. Chan JC, Oyler NA, Yau WM, Tycko R. Parallel  $\beta$ -sheets and polar zippers in amyloid fibrils formed by residues 10-39 of the yeast prion protein Ure2p. *Biochemistry* 2005;44:10669–10680. [PubMed: 16060675]
9. Shewmaker F, Wickner RB, Tycko R. Amyloid of the prion domain of Sup35p has an in-register parallel  $\beta$ -sheet structure. *Proc. Natl. Acad. Sci. U.S.A* 2006;103:19754–19759. [PubMed: 17170131]
10. Török M, Milton S, Kayed R, Wu P, McIntire T, Glabe CG, Langen R. Structural and dynamic features of Alzheimer's A $\beta$  peptide in amyloid fibrils studied by site-directed spin labeling. *J. Biol. Chem* 2002;277:40810–40805. [PubMed: 12181315]
11. Der-Sarkissian A, Jao CC, Chen J, Langen R. Structural organization of alpha-synuclein fibrils studied by site-directed spin labeling. *J. Biol. Chem* 2003;278:37530–37535. [PubMed: 12815044]
12. Luca S, Yau WM, Leapman R, Tycko R. Peptide conformation and supramolecular organization in amylin fibrils: constraints from solid-state NMR. *Biochemistry* 2007;46:13505–13522. [PubMed: 17979302]
13. Balbach JJ, Ishii Y, Antzutkin ON, Leapman RD, Rizzo NW, Dyda F, Reed J, Tycko R. Amyloid fibril formation by A $\beta$ 16-22, a seven-residue fragment of the Alzheimer's  $\beta$ -amyloid peptide, and structural characterization by solid state NMR. *Biochemistry* 2000;39:13748–13759. [PubMed: 11076514]
14. Petkova AT, Buntkowsky G, Dyda F, Leapman RD, Yau WM, Tycko R. Solid state NMR reveals a pH-dependent antiparallel beta-sheet registry in fibrils formed by a  $\beta$ -amyloid peptide. *J. Mol. Biol* 2004;335:247–260. [PubMed: 14659754]
15. Gordon DJ, Balbach JJ, Tycko R, Meredith SC. Increasing the amphiphilicity of an amyloidogenic peptide changes the  $\beta$ -sheet structure in the fibrils from antiparallel to parallel. *Biophys. J* 2004;86:428–434. [PubMed: 14695285]
16. Lansbury PT Jr, Costa PR, Griffiths JM, Simon EJ, Auger M, Halverson KJ, Kocisko DA, Hendsch ZS, Ashburn TT, Spencer RG. Structural model for the  $\beta$ -amyloid fibril based on

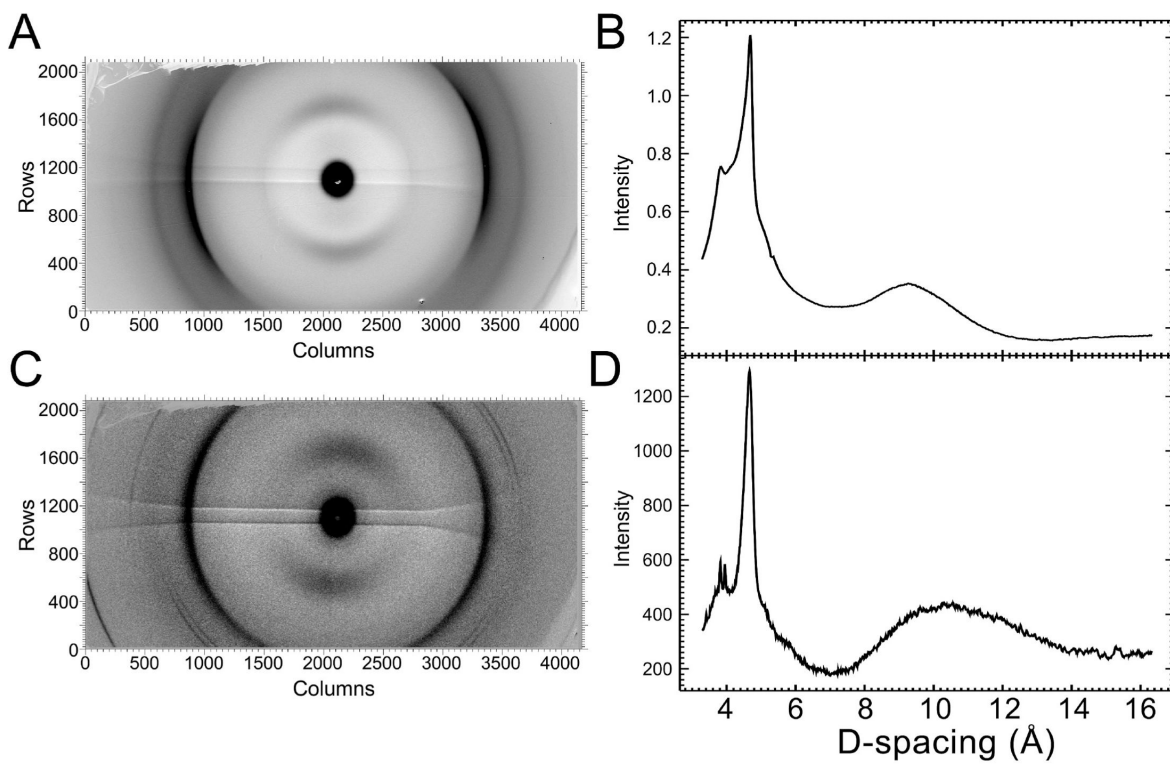
- interstrand alignment of an antiparallel-sheet comprising a C-terminal peptide. *Nat. Struct. Biol.* 1995;2:990–998. [PubMed: 7583673]
17. Goldsbury CS, Wirtz S, Müller SA, Sunderji S, Wicki P, Aebi U, Frey P. Studies on the in vitro assembly of  $\text{A}\beta$ 1-40: implications for the search for  $\text{A}\beta$  fibril formation inhibitors. *J. Struct. Biol.* 2000;130:217–231. [PubMed: 10940227]
  18. Petkova AT, Ishii Y, Balbach JJ, Antzutkin ON, Leapman RD, Delaglio F, Tycko R. A structural model for Alzheimer's  $\beta$ -amyloid fibrils based on experimental constraints from solid state NMR. *Proc. Natl. Acad. Sci. U.S.A.* 2002;99:16742–16747. [PubMed: 12481027]
  19. Petkova AT, Yau WM, Tycko R. Experimental constraints on quaternary structure in Alzheimer's  $\beta$ -amyloid fibrils. *Biochemistry* 2006;45:498–512. [PubMed: 16401079]
  20. Sciarretta KL, Gordon DJ, Petkova AT, Tycko R, Meredith SC.  $\text{A}\beta$ 40-lactam(D23/K28) models a conformation highly favorable for nucleation of amyloid. *Biochemistry* 2005;44:6003–6014. [PubMed: 15835889]
  21. Fraser PE, Nguyen JT, Inouye H, Surewicz WT, Selkoe DJ, Podlisny MB, Kirschner DA. Fibril formation by primate, rodent, and Dutch-hemorrhagic analogues of Alzheimer's amyloid  $\beta$ -protein. *Biochemistry* 1992;31:10716–10723. [PubMed: 1420187]
  22. van Nostrand W, Melchor JP, Cho HS, Greenberg SM, Rebeck GW. Pathogenic effects of D23N Iowa mutant amyloid  $\beta$ -protein. *J. Biol. Chem.* 2001;276:32860–32866. [PubMed: 11441013]
  23. Grabowski TJ, Cho HS, Vonsattel JP, Rebeck GW, Greenberg SM. Novel amyloid precursor protein mutation in an Iowa family with dementia and severe cerebral amyloid angiopathy. *Ann. Neurol.* 2001;49:697–705. [PubMed: 11409420]
  24. Kumar-Singh S, Julliams A, Nuydens R, Ceuterick C, Labeur C, Serneels C, Vennekens K, Van Osta P, Geerts H, De Strooper B, Van Broekhoven C. In vitro studies of Flemish, Dutch and wild-type  $\beta$ -amyloid provide evidence for two-staged toxicity. *Neurobiol. Dis.* 2002;11:330–340. [PubMed: 12505425]
  25. Miravelle L, Tokuda T, Chiarle R, Giaccone G, Bugiani O, Tagliavini F, Frangione B, Ghiso J. Substitutions at codon 22 of Alzheimer's  $\text{A}\beta$  peptide induce diverse conformational changes and apoptotic effects in human cerebral endothelial cells. *J. Biol. Chem.* 2000;275:27110–27116. [PubMed: 10821838]
  26. Sian AK, Frears ER, El-Agnaf OMA, Patel BP, Manca MF, Siligardi G, Hussain R, Austen BM. Oligomerization of  $\beta$ -amyloid of the Alzheimer's and Dutch-cerebral-hemorrhage types. *Biochem. J.* 2000;349:299–308. [PubMed: 10861242]
  27. Soto C, Castano EM, Frangione B, Inestrosa NC. The R-helical and  $\beta$ -strand transition in the amino-terminal fragment of amyloid  $\beta$ -peptide modulates amyloid formation. *J. Biol. Chem.* 1995;270:3063–3067. [PubMed: 7852387]
  28. Davis J, van Nostrand WE. Enhanced pathologic properties of Dutch-type mutant amyloid  $\beta$ -protein. *Proc. Natl. Acad. Sci. U.S.A.* 1996;93:2996–3000. [PubMed: 8610157]
  29. Walsh DM, Lomakin A, Benedek GB, Condron MM, Teplow DB. Amyloid  $\beta$ -protein fibrillogenesis. *J. Biol. Chem.* 1997;272:22364–22372. [PubMed: 9268388]
  30. Esler WP, Felix AM, Stimson ER, Lachenmann MJ, Ghilardi JR, Lu Y-A, Vinters HV, Mantyh PW, Lee JP, Maggio JE. Activation barriers to structural transition determine deposition rates of Alzheimer's disease  $\text{A}\beta$  amyloid. *J. Struct. Biol.* 2000;130:174–182. [PubMed: 10940224]
  31. Melchor JP, McVoy L, Van Nostrand WE. Charge alterations of E22 enhance the pathogenic properties of Amyloid  $\beta$ -protein. *J. Neurochem.* 2000;74:2209–2212. [PubMed: 10800967]
  32. Nilsberth C, Westlind-Danielsson A, Eckman CB, Condron MM, Axelman K, Forsell C, Stenh C, Luthman J, Teplow DB, Younkin SG, Naslund J, Lannfelt L. The "arctic" APP mutation (E693G) causes Alzheimer's disease by enhanced  $\text{A}\beta$  protofibril formation. *Nat. Neurosci.* 2001;4:887–893. [PubMed: 11528419]
  33. Tomiyama T, Nagata T, Shimada H, Teraoka R, Fukushima A, Kanemitsu H, Takuma H, Kuwano R, Imagawa M, Ataka S, Wada Y, Yoshioka E, Nishizaki T, Watanabe Y, Mori H. A new amyloid  $\beta$  variant favoring oligomerization in Alzheimer's-type dementia. *Ann. Neurol.* 2008;63:377–387. [PubMed: 18300294]
  34. Scott D. On optimal and data-based histograms. *Biometrika* 1979;66:605–610.

35. Stubbs G. Developments in fiber diffraction. *Curr. Opin. Struct. Biol* 1999;9:615–619. [PubMed: 10508775]
36. Torbet J. Using magnetic orientation to study structure and assembly. *Trends Biochem. Sci* 1987;12:327–330.
37. Bennett AE, Rienstra CM, Auger M, Lakshmi KV, Griffin RG. Heteronuclear decoupling in rotating solids. *J. Chem. Phys* 1995;103:6951–6958.
38. Tycko R. Symmetry-based constant-time homonuclear dipolar recoupling in solid state NMR. *J. Chem. Phys* 2007;126:064506-1–064506-9. [PubMed: 17313228]
39. Ishii Y, Balbach JJ, Tycko R. Measurement of dipole-coupled lineshapes in a many-spin system by constant-time two-dimensional solid state NMR with high-speed magic-angle spinning. *Chem. Phys* 2001;266:231–236.
40. Gullion T, Schaefer J. Rotational-echo double-resonance NMR. *J. Magn. Reson* 1989;81:196–200.
41. Anderson RC, Gullion T, Joers JM, Shapiro M, Edwin Villhauer EB, Weber. Conformation of [ $1\text{-}^{13}\text{C}, {^{15}\text{N}}$ ] acetyl-l-carnitine. Rotational-echo, double-resonance nuclear magnetic resonance spectroscopy. *J. Am. Chem. Soc* 1995;117:10546–10550.
42. Jaroniec CP, Toungle BA, Herzfeld J, Griffin RG. Frequency selective heteronuclear dipolar recoupling in rotating solids: accurate  $^{13}\text{C}$ - $^{15}\text{N}$  distance measurements in uniformly  $^{13}\text{C}$ ,  $^{15}\text{N}$ -labeled peptides. *J. Am. Chem. Soc* 2001;123:3507–3519. [PubMed: 11472123]
43. Petkova AT, Tycko R. Sensitivity enhancement in structural measurements by solid state NMR through pulsed spin locking. *J. Magn. Reson* 2002;155:293–299. [PubMed: 12036340]
44. Bennett AE, Rienstra CM, Griffiths JM, Zhen W, Lansbury PT Jr, Griffin RG. Homonuclear radio frequency-driven recoupling in rotating solids. *J. Chem. Phys* 1998;108:9463–9479.
45. Ishii Y.  $^{13}\text{C}$ - $^{13}\text{C}$  dipolar recoupling under very fast magic angle spinning in solid state nuclear magnetic resonance: applications to distance measurements, spectral assignments, and high-throughput secondary-structure determination. *J. Chem. Phys* 2001;114:8473–8483.
46. Morcombe CR, Gaponenko V, Byrd RA, Zilm KW.  $^{13}\text{C}$  CPMAS spectroscopy of deuterated proteins: CP dynamics, line shapes, and T1 relaxation. *J. Am. Chem. Soc* 2005;127:397–404. [PubMed: 15631490]
47. Takegoshi K, Nakamura S, Terao T.  $^{13}\text{C}$ - $^1\text{H}$  dipolar assisted rotational resonance in magic-angle spinning NMR. *Chem. Phys. Lett* 2001;344:631–637.
48. Paravastu AK, Petkova AT, Tycko R. Polymorphic fibril formation by residues 10-40 of the Alzheimer's  $\beta$ -amyloid peptide. *Biophys. J* 2006;90:4618–4629. [PubMed: 16565054]
49. Wasmer C, Lange A, Van Melckebeke H, Siemer AB, Riek R, Meier BH. Amyloid fibrils of the HET-s(218-289) prion form a beta solenoid with a triangular hydrophobic core. *Science* 2008;319:1523–1526. [PubMed: 18339938]
50. Wishart DS, Bigam CG, Holm A, Hodges RS, Sykes BD.  $^1\text{H}$ ,  $^{13}\text{C}$  and  $^{15}\text{N}$  random coil NMR chemical shifts of the common amino acids. I. Investigations of nearest-neighbor effects. *J. Biomol. NMR* 1995;5:67–81. [PubMed: 7881273]
51. Vinters HV. Cerebral amyloid angiopathy. A critical review. *Stroke* 1987;18:311–324. [PubMed: 3551211]
52. Mandybur TI. The incidence of cerebral amyloid angiopathy in Alzheimer's disease. *Neurology* 1975;25:120–126. [PubMed: 46597]
53. Joachim CL, Morris JH, Selkoe DJ. Clinically diagnosed Alzheimer's disease: autopsy results in 150 cases. *Ann. Neurol* 1988;24:50–56. [PubMed: 3415200]
54. Greenberg SM, Rebeck GW, Vonsattel JPG, Gomez-Isla T, Hyman BT. Apolipoprotein E  $\epsilon$ 4 and cerebral hemorrhage associated with amyloid angiopathy. *Ann. Neurol* 1995;38:254–259. [PubMed: 7654074]
55. Gilbert JJ, Vinters HV. Cerebral amyloid angiopathy: incidence and complications in the aging brain. I. Cerebral hemorrhage. *Stroke* 1983;14:915–923. [PubMed: 6658995]



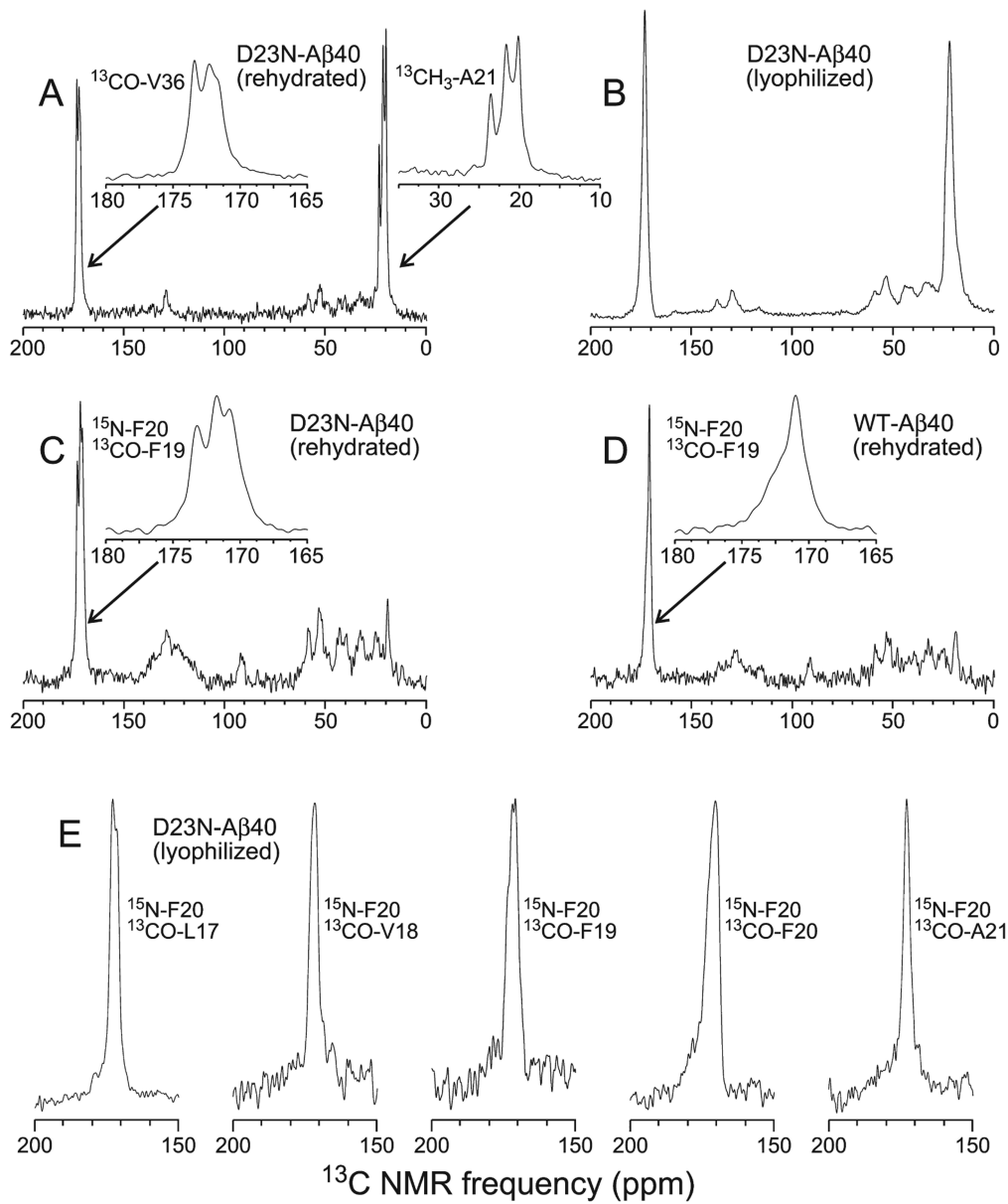
**Figure 1.**

(A) Fibrillogenesis kinetics for D23N-A $\beta$ 40, as measured by thioflavin T fluorescence. Points are experimental data, and the line is a nonlinear least-squares fit to a monoexponential growth, with rate constant  $k = 3.77 \times 10^{-3} \text{ min}^{-1}$ . (B-D) Negatively stained TEM images of D23N-A $\beta$ 40 fibrils, showing the coexistence of fibrils with twisted (single-headed arrows) and untwisted (double-headed arrows) morphologies.

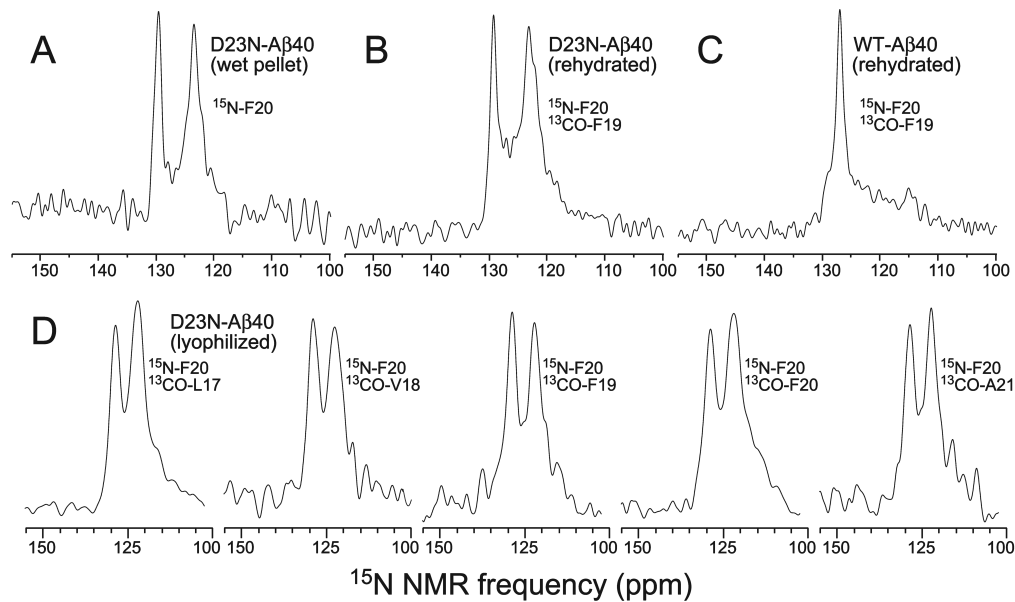


**Figure 2.**

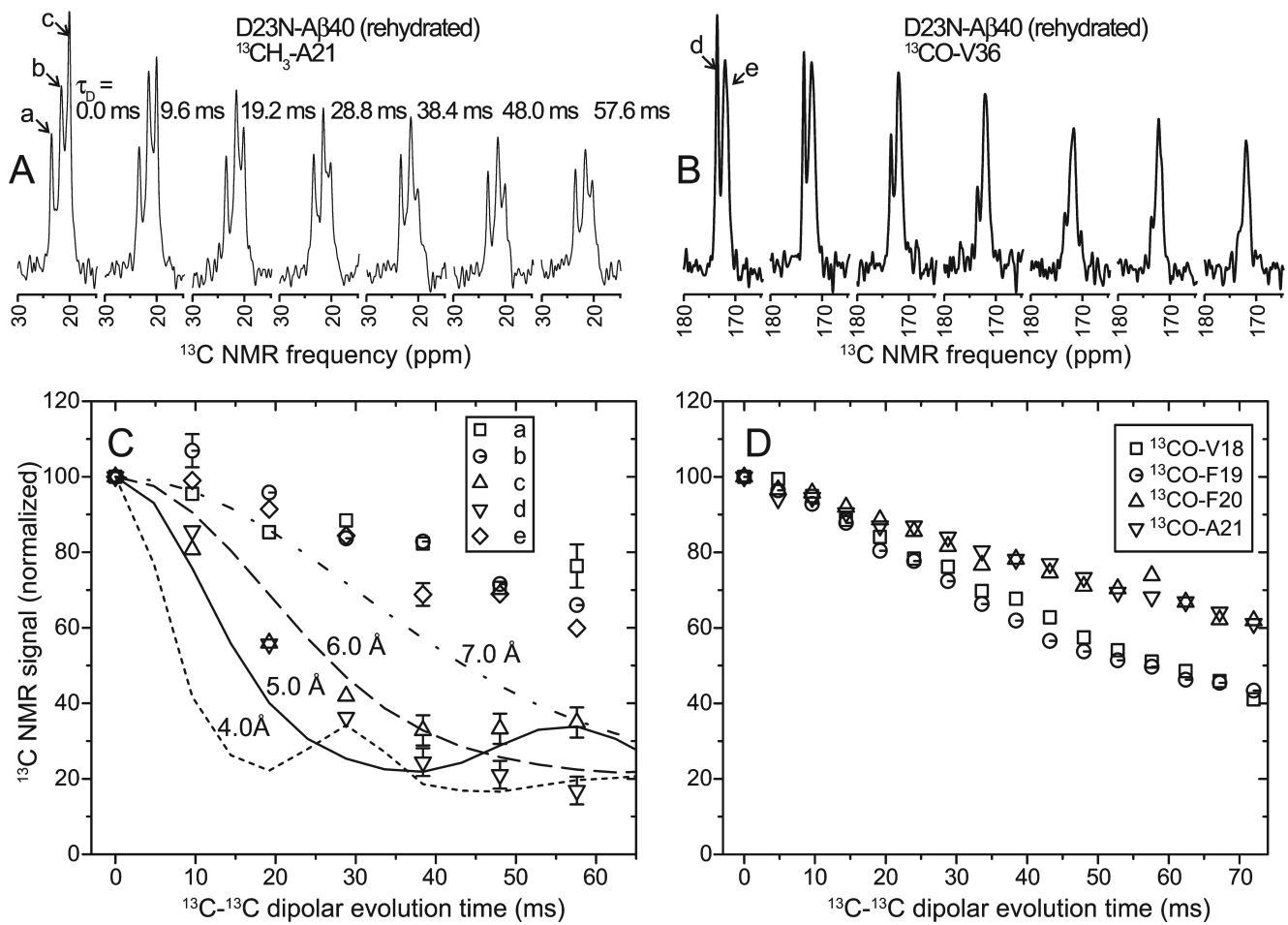
X-ray fiber diffraction patterns for partially aligned fibrils of D23N-A $\beta$ 40 (A) and WT-A $\beta$ 40 (B). For raw data on the left, fibrils are aligned horizontally. Plots on the right are rotationally averaged representations of X-ray scattering intensity as a function of D-spacing.

**Figure 3.**

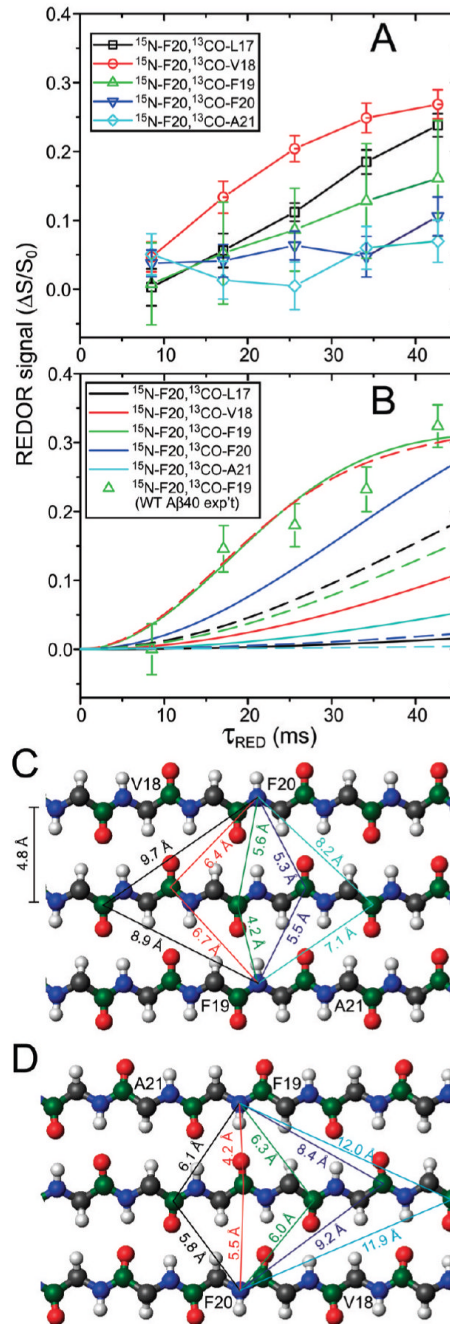
(A, B) <sup>13</sup>C NMR spectra of D23N-A $\beta$ 40 fibrils with <sup>13</sup>C labels at Val36 carbonyl and Ala21 methyl sites, in rehydrated and lyophilized conditions. (C) Spectrum of rehydrated D23N-A $\beta$ 40 fibrils with <sup>15</sup>N labels at Phe20 amide sites and <sup>13</sup>C labels at Phe19 carbonyl sites (1:1 mixture). (D) Spectrum of rehydrated WT-A $\beta$ 40 fibrils with <sup>15</sup>N labels at Phe20 amide sites and <sup>13</sup>C labels at Phe19 carbonyl sites (1:1 mixture). (E) Spectra of lyophilized D23N-A $\beta$ 40 fibrils with <sup>15</sup>N labels at Phe20 amide sites and <sup>13</sup>C labels at the indicated carbonyl sites.

**Figure 4.**

(A)  $^{15}\text{N}$  NMR spectrum of D23N-A $\beta$ 40 fibrils with  $^{15}\text{N}$  at Phe20, without lyophilization.  
 (B) Spectrum of D23N-A $\beta$ 40 fibrils with  $^{15}\text{N}$  at Phe20 and  $^{13}\text{C}$  at Phe19 (1:1 mixture), rehydrated after lyophilization. (C) Spectrum of WT-A $\beta$ 40 fibrils with  $^{15}\text{N}$  at Phe20 and  $^{13}\text{C}$  at Phe19, rehydrated after lyophilization. (D) Spectra of lyophilized D23N-A $\beta$ 40 fibrils with  $^{15}\text{N}$  at Phe20 and  $^{13}\text{C}$  at indicated sites.

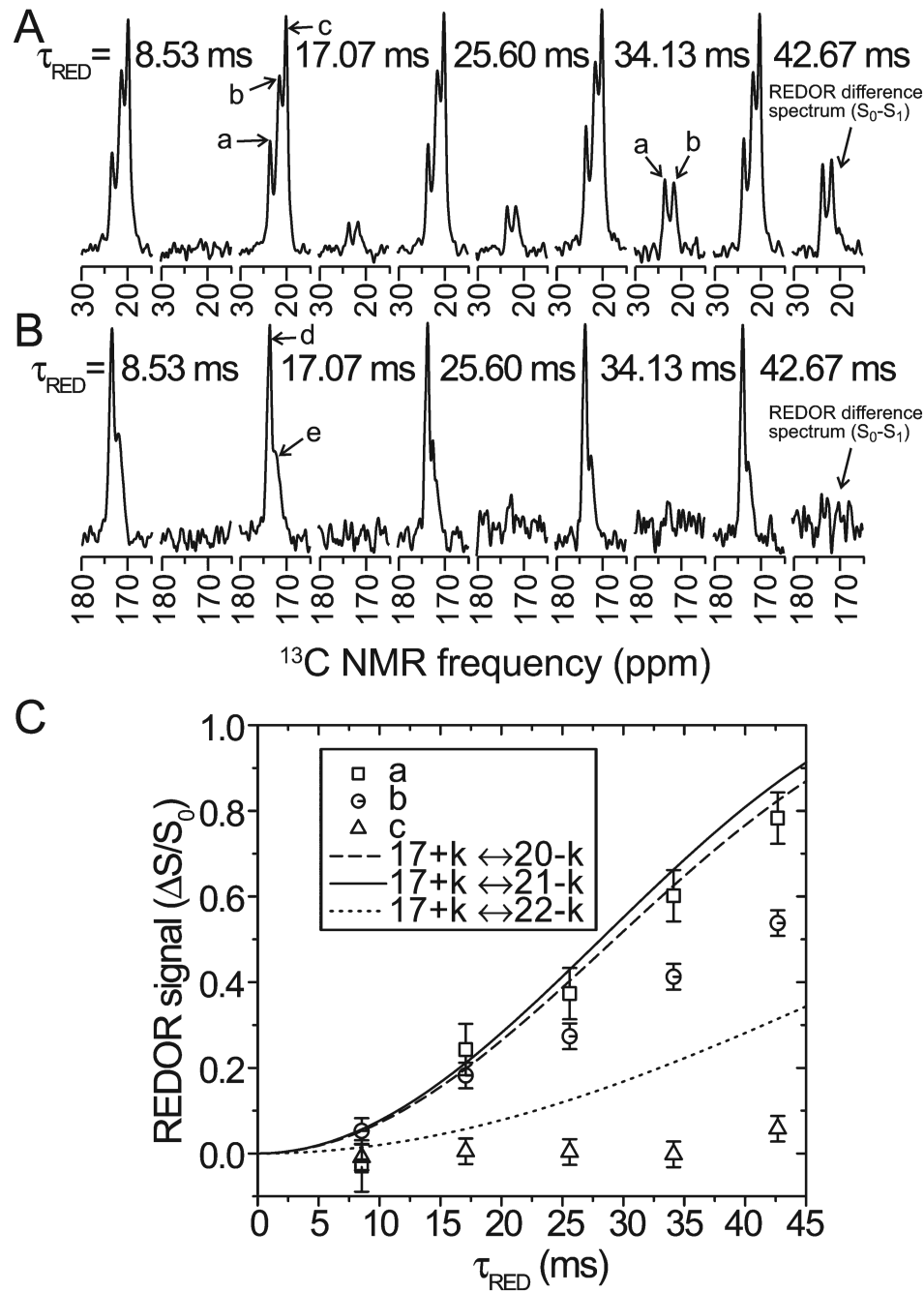
**Figure 5.**

(A, B) Raw PITHIRDS-CT data for rehydrated D23N-A $\beta$ 40 fibrils with  $^{13}\text{C}$  labels at Val36 carbonyl and Ala21 methyl sites. (C) Comparison of  $^{13}\text{C}$  NMR peak areas from PITHIRDS-CT data with simulations for linear chains of  $^{13}\text{C}$  nuclei with the indicated spacings. Only peaks labeled c and d show the rapid signal decay indicative of an in-register, parallel  $\beta$ -sheet structure. (D) Experimental fpRFDR-CT data for lyophilized D23N-A $\beta$ 40 fibrils with  $^{15}\text{N}$  at Phe20 and  $^{13}\text{C}$  at carbonyl sites of the indicated residues (1:1 mixtures).

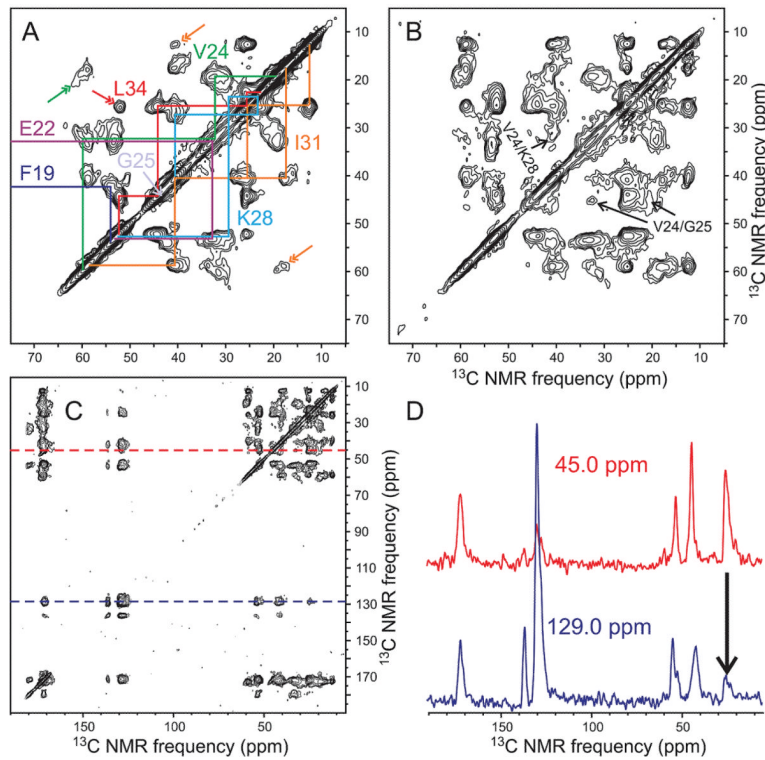
**Figure 6.**

(A)  $^{13}\text{C}$ -detected  $^{15}\text{N}$ - $^{13}\text{C}$  REDOR data for lyophilized D23N-A $\beta$ 40 fibrils with  $^{15}\text{N}$  at Phe20 and  $^{13}\text{C}$  at carbonyl sites of the indicated residues (1:1 mixtures). (B) Simulated REDOR data for fibrils with the indicated label (1:1) mixtures, assuming an in-register, parallel  $\beta$ -sheet structure (solid lines) or an antiparallel  $\beta$ -sheet structure with  $17 + k \leftrightarrow 21 - k$  registry of intermolecular hydrogen bonds (dashed lines). Triangles are experimental data for WT-A $\beta$ 40 fibrils, which are known to contain in-register, parallel  $\beta$ -sheets. (C) Model for an in-register, parallel  $\beta$ -sheet used for REDOR simulations. Relevant distances between Phe20 amide nitrogens (top and bottom chains) and backbone carbonyl sites (middle chain)

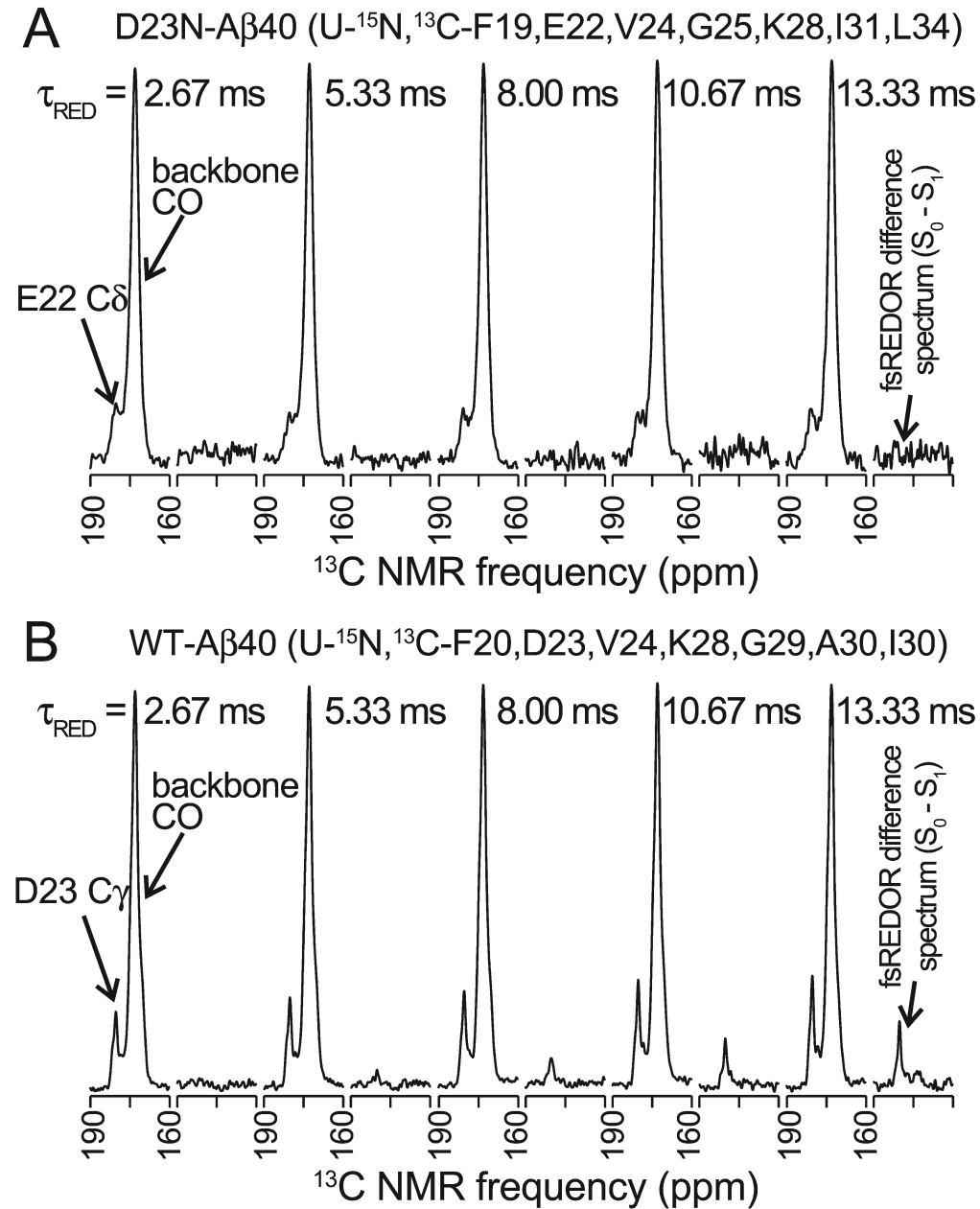
are shown, with color coding to match panel B. (D) Model for an antiparallel  $\beta$ -sheet with  $17 + k \leftrightarrow 21 - k$  registry.

**Figure 7.**

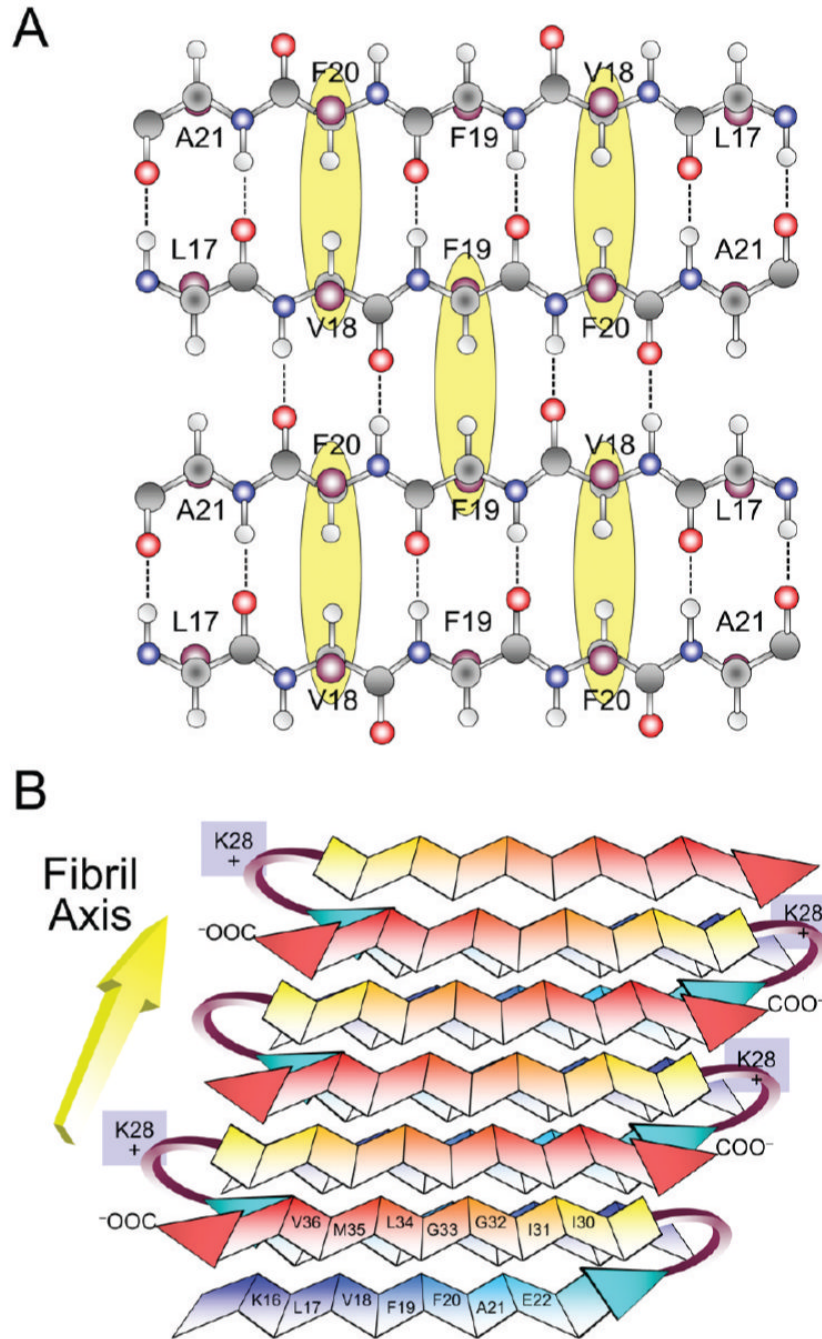
(A, B) Raw <sup>13</sup>C-detected <sup>15</sup>N-<sup>13</sup>C REDOR data for D23N-A<sup>β</sup>40 fibrils with <sup>13</sup>C labeling of Val36 carbonyl and Ala21 methyl sites and <sup>15</sup>N labeling of Leu17 amide sites. For each value of the REDOR dephasing period  $\tau_{\text{RED}}$ , methyl (A) and carbonyl (B) regions of  $S_0$  and  $S_0 - S_1$  difference spectra are shown. Significant signal in the difference spectrum appears only for methyl peaks a and b. (C) Comparison of experimental REDOR signals for Ala21 methyl peaks (symbols) with simulations for antiparallel  $\beta$ -sheet structures with the indicated hydrogen bond registries.

**Figure 8.**

(A) Aliphatic region of 2D <sup>13</sup>C-<sup>13</sup>C NMR spectrum of rehydrated D23N-A $\beta$ 40 fibrils with uniform <sup>15</sup>N,<sup>13</sup>C labeling of Phe19, Glu22, Val24, Gly25, Lys28, Ile31, and Leu34. Chemical shift assignment paths are shown. This spectrum was obtained with fpRFDR mixing for 2.232 ms. (B, C) 2D <sup>13</sup>C-<sup>13</sup>C NMR spectrum of the same sample, obtained with RAD mixing for 500 ms. (D) 1D slices of the 2D RAD spectrum at indicated chemical shift positions, showing the Phe19/Leu34 cross-peak.

**Figure 9.**

(A) Raw fsREDOR data for rehydrated D23N-A $\beta$ 40 fibrils with uniform  $^{15}\text{N}$ ,  $^{13}\text{C}$  labeling of indicated residues. For each value of the fsREDOR dephasing period,  $\tau_{\text{RED}}$ , carbonyl regions of  $S_0$  and  $S_0 - S_1$  difference spectra are shown. The difference spectra show no signals above the noise. (B) Raw fsREDOR data for rehydrated WT-A $\beta$ 40 fibrils, with uniform  $^{15}\text{N}$ ,  $^{13}\text{C}$  labeling of indicated residues. The difference spectra show strong signals from Asp23 side chain carboxyl groups, resulting from close proximity to Lys28 side chain amine groups in Asp23/Lys28 salt bridges.

**Figure 10.**

Hypothetical model for D23N-A $\beta$ 40 fibrils with antiparallel  $\beta$ -sheet structures. (A) Antiparallel  $\beta$ -sheet structure, with  $17 + k \leftrightarrow 21 - k$  registry of intermolecular hydrogen bonds. (B) Hypothetical structure of a molecular layer of the fibril, showing two antiparallel  $\beta$ -sheets in each layer. Data from 2D RAD indicate that the side chains of F19 and L34 are in proximity, although it is not known whether the contact is intra- or intermolecular. The exact length and position of the two  $\beta$ -strands (red and blue) are not known; the N-terminus of the peptide is not shown. Solid-state NMR data indicate that residues 16-22 are within the N-terminal  $\beta$ -strand and residue L34 is within the C-terminal  $\beta$ -strand. The depiction of several other residues in a C-terminal  $\beta$ -sheet is hypothetical, since the antiparallel

alignment of a potential C-terminal  $\beta$ -sheet has not been proven. The figure also indicates a hypothetical interaction between the C-terminal carboxyl group and the side chain of K28; an additional interaction could occur between the side chains of E22 and K16 (not shown). Validation and further refinement of this model will require additional experiments.

<sup>13</sup>C NMR Chemical Shifts in Spectra of D23N- $\text{A}\beta$ 40 Fibrils<sup>a</sup>

Table 1

peptide	residue	CO	C $\alpha$	C $\beta$	C $\gamma$	C $\delta$	C $\epsilon$	C $\zeta$
D23N	F19	171.9	54.2	42.3	136.7	129.6		
RC	F19	174.1	56.0	37.9	137.2	130.2	129.8	128.2
$\partial\ \partial$	F19	2.2	1.8	-4.4				
D23N	E22	172.1	~52.8	~30.2	33.9	180.7		
RC	E22	174.9	54.9	28.2	33.9	181.7		
$\partial\ \partial$	E22	2.8	2.1	-1.4				
D23N	V24	173.2, 173.2	60.4, 59.1	31.5, 33.4	20.5			
RC	V24	174.6	60.5	31.2	19.4, 18.6			
$\partial\ \partial$		1.4	0.1, 1.4	-0.3, 2.2				
D23N	G25	171.7	43.8					
RC	G25	173.2	43.4					
$\partial\ \partial$	G25	1.5	-0.4					
D23N	K28	172.1	53.2	~32.8	~22.6	27.2	40.6	
RC	K28	174.9	54.5	31.4	23.0	27.3	40.2	
$\partial\ \partial$	K28	2.8	1.3	-1.4				
D23N	L34	172.3	52.4	44.4	25.4	~23.3		
RC	L34	175.9	53.4	40.7	25.2	23.2, 21.6		
$\partial\ \partial$	L34	3.6	1.0	-3.7				

<sup>a</sup><sup>13</sup>C NMR chemical shifts (ppm, relative to tetramethylsilane) in spectra of D23N- $\text{A}\beta$ 40 fibrils. For comparison, values are given for random coil peptides, from Wishart et al. (50), adjusted to the tetramethylsilane reference by subtracting 1.7 ppm. The secondary chemical shift,  $\Delta\delta$ , is defined as the difference between the chemical shift for a random coil and that for D23N- $\text{A}\beta$ 40, i.e.,  $\Delta\delta = \delta_{\text{D23N}} - \delta_{\text{RC}}$ . Shifts that follow the trend for  $\beta$ -sheets have deviations greater than 0.5 ppm from random coil values, negative for CO and C $\alpha$  and positive for C $\beta$ . In general, chemical shift values are accurate to within  $\pm 0.1$  ppm; for Glu22 and Lys28, some of the peaks were broad and of low intensity, and the values reported are  $\pm 0.5$  ppm.